USAF/EOARD
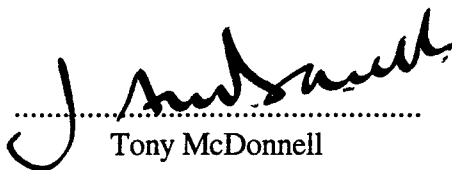## Research Contract F61708-95-C0011

Investigation of Energy Partitioning in Hypervelocity Impacts

Final Report

J.~~~~~~~~
....
Tony McDonnell
Principal Investigator

....
Paul Ratcliff
Co-Investigator

19990204 028

Unit for Space Sciences and Astrophysics
University of Kent at Canterbury

AQF-99-05-0843

REPORT DOCUMENTATION PAGE

Form Approved OMB No. 0704-0188

1. AGENCY USE ONLY (Leave blank)	2. REPORT DATE September 1996	3. REPORT TYPE AND DATES COVERED Final Report

4. TITLE AND SUBTITLE

Investigation of Energy Partitioning in Hypervelocity Impacts

5. FUNDING NUMBERS

F6170895C0011

6. AUTHOR(S)

Dr. J.A.M. McDonnell

7. PERFORMING ORGANIZATION NAME(S) AND ADDRESS(ES)

University of Kent
Unit for Space Sciences and Astrophysics
The University
Canterbury CT2 7NR
United Kingdom

8. PERFORMING ORGANIZATION REPORT NUMBER

N/A

9. SPONSORING/MONITORING AGENCY NAME(S) AND ADDRESS(ES)

EOARD
PSC 802 BOX 14
FPO 09499-0200

10. SPONSORING/MONITORING AGENCY REPORT NUMBER

SPC 95-4031

11. SUPPLEMENTARY NOTES

12a. DISTRIBUTION/AVAILABILITY STATEMENT

Approved for public release; distribution is unlimited.

12b. DISTRIBUTION CODE

A

13. ABSTRACT (Maximum 200 words)

This report results from a contract tasking University of Kent as follows: The need to understand the physics of, and to define the parameters of, energy partitioning in the impact processes at very high velocities led to a research thrust focused on the 2 MV Van de Graaf facility at Kent. A key basis for this research is summarised in the published IAF paper (Ratcliff et all., Appendix A) where the measurement of impact plasma and momentum leading to derivation of ejecta kinetic energy is described.

14. SUBJECT TERMS

EOARD

15. NUMBER OF PAGES

55

16. PRICE CODE

N/A

17. SECURITY CLASSIFICATION OF REPORT UNCLASSIFIED	18. SECURITY CLASSIFICATION OF THIS PAGE UNCLASSIFIED	19. SECURITY CLASSIFICATION OF ABSTRACT UNCLASSIFIED	20. LIMITATION OF ABSTRACT UL

CONTENTS

Page

P.R. Ratcliff, M.J. Cole, J.A.M. McDonnell, H.A. Shaw and F. Allahdadi, 'Experimental Determination of Energy Partitioning in Microparticle Impacts at Velocities from 1 to 100 kms^{-1}', paper IAF-95-I.5.03, presented at the 46th International Astronautical Congress, October 2-6, 1995, Oslo, Norway.

P.R. Ratcliff, M.J. Burchell, M.J. Cole, T.W. Murphy and F. Allahdadi, 'Experimental Measurements of Hypervelocity Impact Plasma Yield and Energetics', *Int. J. Impact Engng* (in press), and to be presented at HVIS '96, Freiberg, Germany.

ABSTRACT

A programme of hypervelocity impact research has been completed by the Unit for Space Sciences and Astrophysics at the University of Kent at Canterbury in accordance with USAF/EOARD Research Contract F61708-95-C0011.   This work, based on experimental investigations using the UNit's 2MV Van de Graaff dust accelerator and hydrocode simulations, had the objective of characterising energy partitioning and momentum exchange during hypervelocity impacts of particles on spacecraft and astrophysical materials.

Based on data obtained during experimental campaigns and reviews of data obtained during the previous research contract (USAF/EOARD F49620-93-1-0487) and in the published literature, equations have been derived which characterise the momentum enhancement for impacts on metallic and meteoritic material, and energy partitioning to three paths (ejecta kinetic energy, light flash and ionisation, the latter subdivided into ion kinetic energy and ionisation energy) for impacts on metallic materials, as a function of impact velocity.

1. INTRODUCTION

The need to understand the physics of, and to define the parameters of, energy partitioning in the impact processes at very high velocities led to a research thrust focused on the 2 MV Van de Graaff facility at Kent. A key basis for this research is summarised in the published IAF paper (Ratcliff et al., Appendix A) where the measurement of impact plasma and momentum leading to derivation of ejecta kinetic energy is described.

In this programme we report an extension of impact parameter measurements, of momentum exchange at impact on laboratory materials and those of astrophysical significance (near-Earth proto-planetary objects); of special interest to future work in the field of planetary defence, where such parameters define the effectiveness of orbital deviations in energy exchanges following interception.

2. EXPERIMENT CONFIGURATIONS

2.1. The Accelerator Facility

The experiment campaigns utilised the Unit's 2 MV Van de Graaff dust accelerator, which is one of only two such facilities in the world (none are in the USA). In this facility micron and sub-micron dust particles are charged and accelerated through a 2 MV potential. A continual stream of particles is provided to the user. Recent (January 1995) enhancements to the instrumentation allow particle velocities up to 120 km s^{-1} to be routinely attained; the record velocity (February 1995) now stands at 215 ± 10 km s^{-1}! The accelerator thus affords the capability of investigating all velocities of relevance to spacecraft applications, including potential impact by interstellar grains at velocities up to 150 km s^{-1}. The particle charge, mass and velocity are measured, and individual particles can be selected according to velocity.

Features distinguishing this accelerator 'from all others' are extremely accurate particle impactor characterisation, economy, and of high astrophysical significance, totally unmatched attainment of realistic space velocities. Of special note, the electrostatic accelerator delivers very well characterised particles in a 'clean' environment, with none of the explosive or radiative phenomena normally associated with the launch of projectiles by other facilities.

Due to the physics of the particle charging process smaller dust grains tend to possess a greater charge-to-mass ratio than larger ones and therefore attain higher velocities in falling through the 2 MV potential drop (Figure 1). There is thus a strong correlation between particle size (or mass) and velocity, and it is important to bear this in mind when performing investigations over a wide range of velocities.

Measurement of the mass and velocity of individual particles is achieved by measuring the induced charge in two tubular electrodes. The typical induced charge is 10^{-12} - 10^{-16}

C. The height of the pulse from the voltage amplifiers attached to the electrodes is proportional to the charge q on the particle and the separation of the pulses is inversely proportional to the velocity v. The mass can then be calculated from:

$$1/2mv^2 = qV_A \qquad (1)$$

where V_A is the accelerating voltage and m is the mass of the projectile. Hence the velocity at a given mass is given by:

$$v = \sqrt{(2qV_A/m)} \qquad (2)$$

the mass at a given velocity by:

$$m = 2qV_A/v^2 \qquad (3)$$

and the radius at given velocity:

$$r^3 = 3qV_A/(2\pi\rho v^2) \qquad (4)$$

where ρ is the material density.
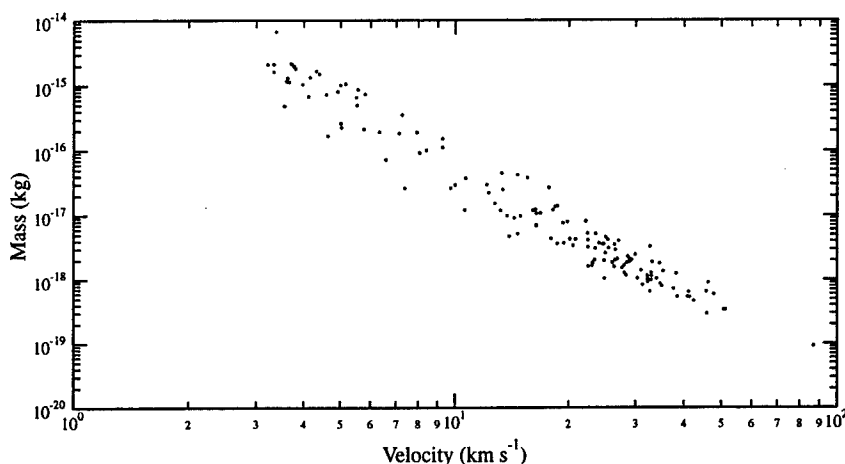
Figure 1. Sample plot of the mass-velocity performance of the dust accelerator (from Ratcliff et al. 1996b).

2.2. Experiment Configurations (Workpackage 1)

2.2.1.Impact Plasma Measurements

Impact plasma measurements were made using the experiment configuration developed under USAF/EOARD Contract F49620-93-1-0487, which was a refinement of the prototype of the Chemical Analyser Subsystem of the Cassini/Huygens Cosmic Dust Analyser (Ratcliff et al. 1992). The experiment configuration is shown in Figure 2. The target assembly was mounted in the small target chamber available at the impact facility, which has an internal diameter of 30 cm and 10 ports at 36° intervals around the side. The accelerator beam line was introduced to the chamber through one of

these ports and the particles allowed to impact on the target. The target itself consisted of a 25 μm thick rhodium foil bonded (with conductive epoxy resin) to a 0.5 mm thick aluminium plate, which was in turn mounted on a perspex block to provide electrical isolation. The target was maintained at a positive potential. A fine grid (150 lines per inch, 85% transparency) was mounted 3.3 mm in front of the target. This was electrically isolated from the target and was earthed. A planar electric field was thus sustained above the surface of the target, which separates the impact plasma.
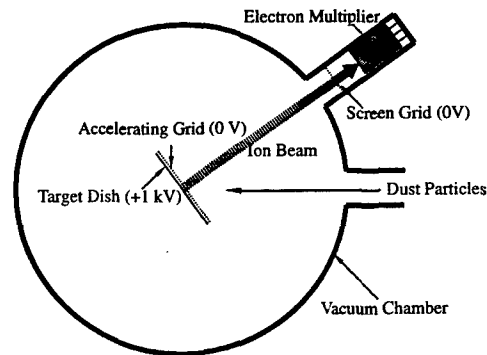

Figure 2. The experiment configuration for the impact plasma measurements (from Ratcliff et al. 1995).

The electrons (and any negative ions) were collected on the target (from which the signal, measured via a charge-sensitive amplifier, gives the integrated ion yield) while the positive ions were accelerated in the direction of the target normal. In order to focus these ions on the electron multiplier, mounted in a tube attached to another of the chamber view ports, the target was mounted at an angle of 36° to the particle beam. This angle is not sufficient to cause elliptical craters to be produced (e.g. Christiansen et al. 1993, McDonnell et al. 1993, Mackay et al. 1993, Hayhurst et al. 1994) and so one would still expect a symmetrical debris cloud thus maintaining the validity for comparison with the normal incidence momentum measurements described below. The purpose of the electron multiplier was to allow time-of-flight mass spectrometric measurements of the impact plasma cloud.

The waveforms recorded from the in-flight electrostatic particle detection, the target and the electron multiplier were recorded on a 4-channel digital storage oscilloscope and transferred to a PC for data analysis and archiving.

An obvious feature of the signals recorded from the target is that they consist of two components (Figure 3). The first component has a very fast risetime (~100-200 ns). Superimposed on this is a much slower signal with a risetime of several μs. The former represents the plasma from the primary impact. The risetime of this signal simply depends on the charge-to-mass ratio of the ions and the strength of the accelerating field. The latter represents ionisation liberated by the impact of ejecta from the primary event on the accelerating grid. The time-constant for this signal depends on the times-of-flight of the ejecta particles. (For a fuller explanation of signal shapes and formation see Ratcliff et al. 1996a). The strength of the accelerating field in these experiments was set to ensure that the two components of the signal were easily resolvable. Initially 1000 V was used. Subsequently two runs were performed using 500 V.
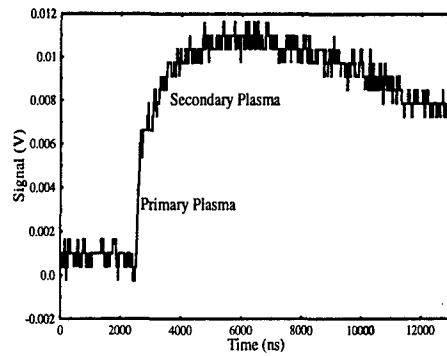
Figure 3. Typical target signal waveform showing the fast-rising primary component and the slower component produced by secondary impacts (from Ratcliff et al. 1995).

2.2.2. Impact Momentum Measurements

The experiment configuration for the impact momentum experiments is shown in Figure 4. A cylindrical piezoelectric crystal 5 mm in diameter and 10 mm long was mounted on a rigid surface using double-sided sticky tape. Electrodes have been deposited on each end of the cylinder. The front surface of the crystal is earthed and the rear surface connected to a voltage amplifier.

The impact target was mounted (with bees' wax, which provides good mechanical coupling but allows ready interchange of targets when heated) on the front surface of the crystal, and was also earthed. Targets were selected to be thick enough to represent a semi-infinite medium to the impacting micron and sub-micron particles but thin enough not to attenuate signals or to allow reflections of the shock waves from the edges of the target to interfere with the primary shock front.
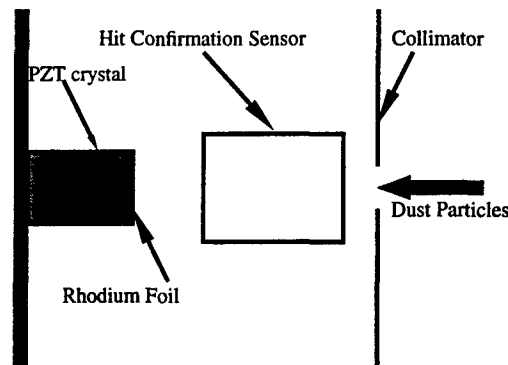
Figure 4. The experiment configuration for the impact momentum measurements (from Ratcliff et al. 1995).

Approximately 25 mm in front of the target a tube was mounted to allow electrostatic detection of incident particles to provide a 'hit confirmation' signal. Immediately in front of this tube was a collimating hole 2.5 mm in diameter which ensured that all events were limited to a confined range on the surface of the crystal. Even so, the sensitivity of the crystal is position-sensitive and so large numbers of events must be recorded and analysed statistically. The characteristics of the incident particle (velocity

5

and charge, and hence mass) were measured by the in-flight electrostatic sensors 'up stream' of the experiment.

2.3. Experiment Campaigns (Workpackage 2)

The following experiment campaigns were performed during this research programme:

Campaign #	Purpose	Result
1	Measurement of secondary ion yield for impacts of iron on rhodium.	Run successfully completed. 142 events recorded.
2	Measurement of momentum enhancement for iron impacts on rhodium.	Run successfully completed. 173 events recorded.
3	Evaluation of PZT sensors.	Run successfully completed. No significant difference in performance noted between different suppliers and/or types.
4	Measurement of momentum enhancement for iron impacts on Zagami meteorite, representing a brittle astrophysical material.	Run successfully completed. 203 events recorded.
5	Measurement of momentum enhancement for boron carbide impacts on glass, representing a brittle but homogeneous material.	Run curtailed due to operational restrictions on the accelerator. 26 events recorded.

2.4. Data Analysis Techniques (Workpackage 3)

Data from the experiment campaigns were recorded on a LeCroy 9304 digitial storage oscilloscope operating at frequencies up to 100 Ms s^{-1}. The data was transferred to an IBM-compatible PC running Labview software for data analysis and archiving.

2.4.1.Impact Plasma Data

The impact plasma data, as shown in Figure 3, needed no special treatment before analysis. The signal-to-noise ratio was good due to the strong signals and low electronic noise of the system, while the relatively long time-constant of the charge-sensitive amplifiers used (~150 μs) meant that no ballistic deficite correction was required even in the case of the slower secondary signals. The primary and secondary ion yields could be derived without difficulty by simple cursor measurement on the stored waveforms.

2.4.2.Momentum Data

Due to the mass-velocity relationship of the particles provided by the UKC dust accelerator facility, the upper limit of velocity achievable for impact momentum measurements is critically dependent on the sensitivity of the transducer used and on the signal-to-noise ratio. Careful design of the electronics used and attention to

mechanical and electrical noise reduction ensured that the limiting noise level was the thermal noise generated by the PZT crystal. A competative analysis of different PZT crystals of different dimensions and materials, and obtained from different manufacturers, ensured that the most sensitive crystal was used, although it was found that crystal dimension was the only significant factor.

The system noise could potentially have been reduced by cooling the PZT transducer, but time and resources did not allow this option to be pursued in the course of the current programme. Instead, efforts were made to optimise the data analysis scheme. In the first run (iron-on-rhodium impacts, run # 2) a narrow band-pass filter was used closely matching the primary resonance frequency of the transducer. This resulted in relatively 'clean' waveforms of the type shown in Figure 5. However, with signals of this form a relatively high signal-to-noise ratio is required in order to identify signals with confidence as the characteristics of a true signal only differ from noise in magnitude (the time-of-impact as calculated from the time-of-flight and hit confirmation sensors provides a useful coincidence signal to aid identification).
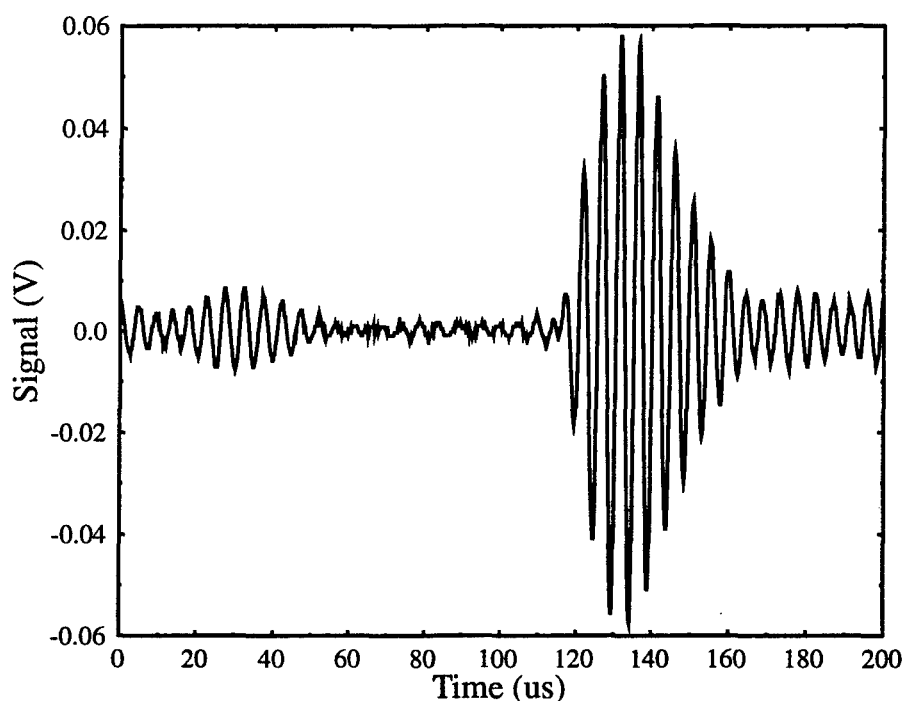
Figure 5. Narrow bandpass-filtered PZT signal from the impact of a 1.8×10^{-14} kg particle at 2.76 kms^{-1} (momentum 4.9×10^{-11} Ns) (from Ratcliff et al. 1995).

During the transducer selection process it was noted that the selected transducer resonates at 4 dominant frequencies. If a narrow bandpass filter were used matched to . the strongest of these frequencies, a significant fraction of the energy deposited in the crystal by the impact would be 'thrown away' in the other frequencies. It was found to be preferable to use a wide bandpass filter (and accept the higher noise levels this entailed) covering the four main frequencies. This has the added advantage of

7

producing a much more easily identifiable signal shape. The impact excites the 4 frequencies in phase with each other, but the phase differences soon cause destructive interference to occur and so the signal adopts the form of a strong first peak followed by a train of much lower, and varying, peaks similar to an enhanced noise level. A fuller explanation of this is given in the contract Monthly Report No. 5, January 1996.

Attempts were made to investigate the use of a digital notch filter matched to the 4 dominant frequencies of the crystal in order to reduce the noise level incurred using a wide bandpass filter, but this could not be implimented in the course of this programme.

3. EXPERIMENTAL RESULTS

3.1. Momentum Enhancement

3.1.1.Theory

During a hypervelocity impact event an impact crater is typically formed, resulting from the ejection of target material from the impact site. If the impact occurs on a semi-infinite target, this ejecta (which will generally also contain material from the projectile) will have a net momentum component in the direction of the target normal and so conservation of momentum dictates that an equal and opposite momentum is imparted to the target. If a momentum sensor is used on the target and has a response time which is long compared with the timescale of ejecta formation, the signal it records will be the sum of the incident particle and the ejecta momenta. Thus:

$$p_{total} = p_p + p_e = p_p(1 + p_e/p_p) = \mathcal{E}p_p \tag{5}$$

where $\mathcal{E}$ is defined as the momentum enhancement. For non-normal particle incidence the momenta are represented by vectors and $\mathcal{E}$ is represented by a diagonal matrix whose leading diagonal elements describe the enhancement in the direction of the target normal and in two perpendicular directions in the target plane. However, for normal incidence impacts, as was the case in this work, it is reasonable to assume that the debris cloud is radially symmetrical about the target normal and so there will be no net momentum parallel to the target plane. Momenta and $\mathcal{E}$ can thus be considered as scalar.

If we consider the two-dimensional distribution of the ejecta cloud then (regarding the impact site as a point source of ejecta) the mass ejected at angle θ is $m_e(\theta)d\theta$ and the component of the momentum in the direction of the target normal is

$$p_e(\theta) = m_e(\theta)d\theta v_e(\theta)\cos\theta \tag{6}$$

where $v_e(\theta)$ is the mean ejecta velocity in direction θ.

Integrating over all ejection angles

$$p_e = \int_0^{\pi/2} m_e(\theta)v_e(\theta)\cos\theta\, d\theta \qquad (7)$$

and hence

$$\mathcal{E} = 1 + \frac{\int_0^{\pi/2} m_e(\theta)v_e(\theta)\cos(\theta)\, d\theta}{p_p} \qquad (8)$$

We can apply constraints to the velocity of the ejecta since conservation of energy demands that the mean velocity of the material ejected into angular segment $d\theta$ satisfies the equation

$$\frac{1}{2}\int_0^{\pi/2} m_e(\theta)\, d\theta \left(\int_0^{\pi/2} v_e(\theta)\, d\theta \right)^2 = \frac{1}{2}m_p v_p^2 - E_d \qquad (9)$$

E_d is the fraction of the incident particle kinetic energy that is not transferred to ejecta kinetic energy. This includes energy 'lost' to material heating, compaction, fragmentation etc. and is loosely referred to as the 'decomposition energy'.

In order to proceed further we must define explicit expressions for $m_e(\theta)$, $v_e(\theta)$ and E_d. For high impact velocities and correspondingly large (with respect to the projectile size) craters the ejecta is dominated by target material and so the volume of ejecta can be approximated by the volume of the crater. This can be estimated using any of the empirical equations in the published literature (e.g. Watts and Atkinson 1994). This defines the mass integrated over θ, but the angular dependence is also significant as this affects the relative magnitudes of the ejecta momentum components normal to and parallel to the plane of the target. Attempts have been made to characterise this dependence, and the angular dependence of v_e, experimentally for a variety of projectile and target materials (e.g. Gault and Heitowit 1963, Eichorn 1978, Thomsen et al. 1980, Croft 1981) and the results of Eichorn (1978) (the only study using metal targets) have been used in the analysis of the iron-on-rhodium data below. If assumptions are made about the angular dependence of m_e and v_e then a 'characteristic' ejecta velocity can be derived from the measurement of the ejecta momentum and the calculation of its mass, and so the ejecta kinetic energy can be estimated.

The assumption is frequently made in momentum enhancement work (e.g. Rembor 1993) that $v_e(\theta)$ and $m_e(\theta)$ are not velocity-dependent. This results in $\mathcal{E}$ being a linear function of impact velocity, though the assumption is not supported by experiment (e.g. Eichorn 1978). Generally, particularly for a ductile target, the ejecta angular distribution tends towards the target normal with increasing impact velocity and so the normal component of the momentum is enhanced with respect to the radial component, resulting in a dependence of momentum enhancement on impact velocity above linearity. This effect is reduced in the case of a brittle target since the mass of ejecta is dominated by spalled material which has a velocity predominantly in the direction of the target normal.

E_d is generally assumed to be proportional to the ejected mass of the target, i.e.

$$E_d = \varepsilon_t \rho_t V_c \qquad (10)$$

The constant of proportionality, ε_t, has the dimensions of specific energy and represents an 'effective decomposition energy'. However, if this assumption is adopted, along with the assumption that crater volumes are proportional to impactor kinetic energy (e.g. Eichorn and Gr,n 1993), it follows that the ejecta kinetic energy represents a constant fraction (i.e. independent of impact velocity) of the impactor kinetic energy. This is obviously not the case, particularly at low impact velocities where little or no ejecta is generated. However, if the kinetic energy of the ejecta is measured by independent means, the 'decomposition energy' can be readily determined.

3.1.2. Results

Iron on Aluminium

An extensive investigation of momentum enhancement for iron micro-particle impacts on aluminium was performed on the UKC dust accelerator facility by Rembor (Rembor, 1993) using 1 mm thick aluminium plates as targets. A relatively wide scatter was observed in the results due to various experimental considerations and, in some cases, poor statistics. Derived values of the threshold velocity ranged from 1.1 to 3.3 km s^{-1} (average 2 km s^{-1}) while the velocity-dependence ranged from 0.2 to 0.37 s km^{-1} (although one result of 0.78 s km^{-1} was obtained), with an average of 0.3 s km^{-1}.

Iron on Rhodium

The measured PZT signals (in V) normalised with respect to the momentum of the incident particle (in Ns) are shown in Figure 6, along with the least-squares fit for the function

$$
\begin{aligned}
S &= a & v < v_o & \qquad (11)\\
S &= a + b(v-v_o) & v > v_o & \qquad (12)
\end{aligned}
$$

A linear fit has been assumed since the scatter on the data and the limited velocity range do not warrant a more complicated function. a represents the PZT sensitivity (mV/Ns) and v_o the threshold velocity for ejecta formation (and hence momentum enhancement).
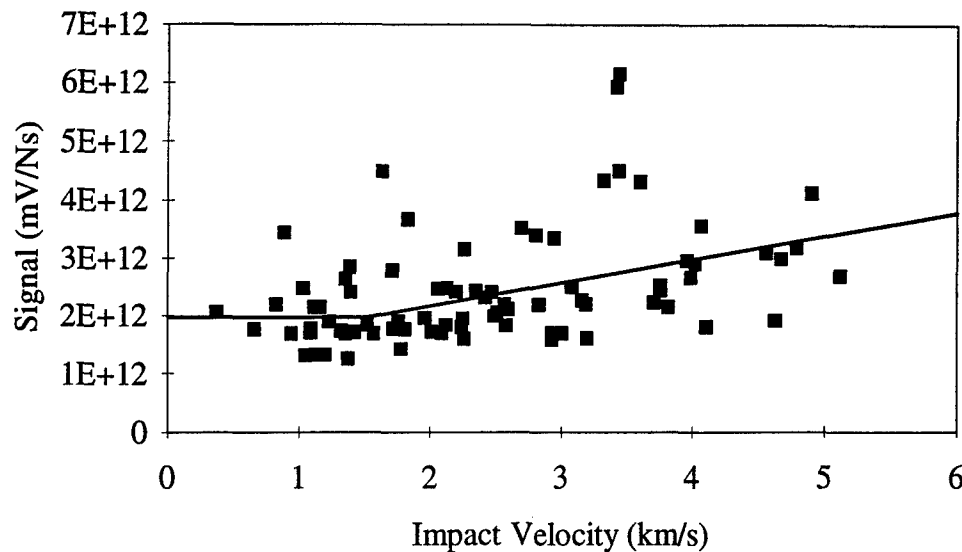
10

Figure 6. PZT signals normalised with respect to the projectile momentum, plotted against impact velocity. The solid line is the least squares fit (from Ratcliff et al. 1995).

The PZT sensitivity was derived as 1.97×10^9 V/Ns. The average rms noise level recorded was 2.9 mV, so a signal-to-noise criterion of 3:1 corresponds to a signal of 8.7 mV and a threshold momentum of 4.4×10^{-12} Ns. For the mass-velocity dependence of the dust accelerator this corresponds to a velocity of ~ 5 kms^{-1}. The fact that some events are recorded above this velocity is due to the statistical variation in particle masses (and hence momenta) at given velocities and to the onset of momentum enhancement.

The threshold velocity v_0 was derived as 1.5 ± 0.2 km s^{-1}. Slattery and Roy (1970) and Stradling et al. (1990) assume the onset of momentum enhancement to occur when the impact velocity exceeds the speed of sound in the material. However, it is well known experimentally that impact plasma (dominated by alkali metal contaminants) is produced at velocities of ~ 1.5 km s^{-1}, and since the production of plasma and/or vapour must clearly produce momentum enhancement in just the same way as production of solid or liquid ejecta does there is no reason why momentum enhancement should be linked to the speed of sound in the material. Our value of 1.5 km s^{-1} is clearly inconsistent with the speed of sound in rhodium, but is consistent with the threshold velocity for impact plasma production and is also in keeping with the findings of Rembor (1993).

Dividing the normalised signals (in Figure 6) by the PZT sensitivity gives the momentum enhancement. This was derived for each event and the average calculated for velocity bins. The results are shown in Figure 7 along with the calculated fit. The observed gradient is 0.21 s km^{-1}. This is in very close agreement with Slattery and Roy (1970) and Stradling et al. (1990), who both derived values of ~ 0.2 s km^{-1}, and with Rembor (1993).
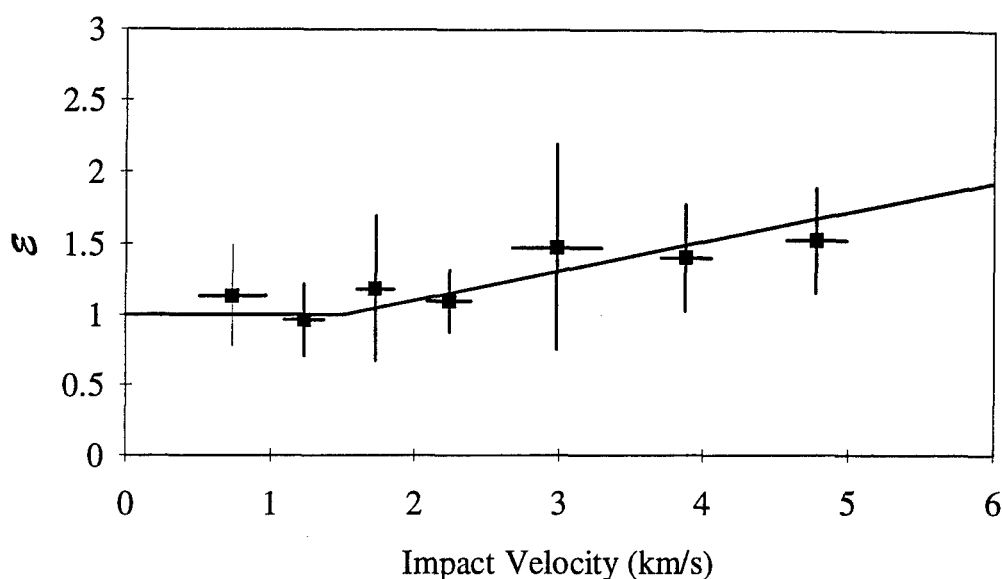
Figure 7. Momentum enhancement for iron microparticle impacts on rhodium. Error bars are the standard deviation of the binned data (from Ratcliff et al. 1995).

Iron on Zagami Meteorite

The Zagami meteorite is a shergotite eucrite achondritic stoney meteorite containing trapped gasses in the same percentages as the material tested by the Viking probes on Mars, and is believed to have come from that planet. It is a very young volcanic rock, with a macroscopic grainy structure. Since the structure is not homogeneous on the scale of the dust particles used for the experimental measurements, it is reasonable to expect the impact site to affect the ejecta production and hence the derived momentum enhancement. This would be reflected in a greater degree of scatter in the data set.

For the Zagami meteorite the PZT sensitivity was derived as 0.6×10^{12} V/Ns (Figure 8), a factor of 3 lower than for the rhodium foil. This is attributed to the greater thickness of the meteorite sample (~ 1 mm compared with 50 μm) and the greater difficulty in ensuring good coupling to the PZT.

The best least-squares fit to the data is a simple linear function with no threshold, indicating that either ejecta is produced at all impact velocities or that the threshold velocity is lower than was covered in the experiment (120 m s^{-1}). This is not unreasonable in view of the brittle nature of the material.

Figure 9 shows the momentum enhancement results for the zagami meteorite sample. The functional form is

$$\mathcal{E} = 1 + 0.35v \tag{13}$$

where v is measured in km s^{-1}. The velocity-dependence of the momentum enhancement is thus much stronger than has been observed for metallic targets.
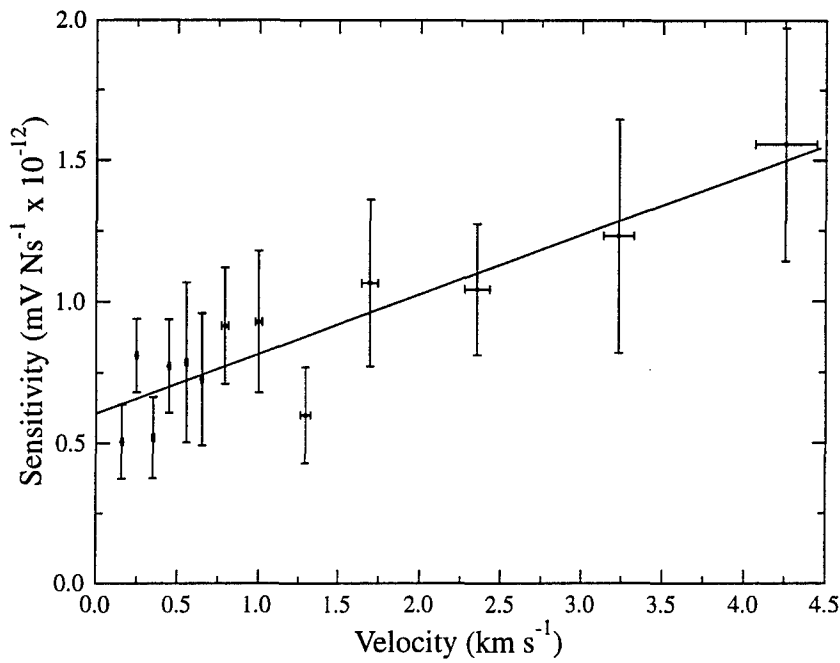
12

Figure 8. PZT signals normalised with respect to the projectile momentum, plotted against impact velocity, for iron microparticle impacts on Zagami meteorite. The solid line is the least squares fit.
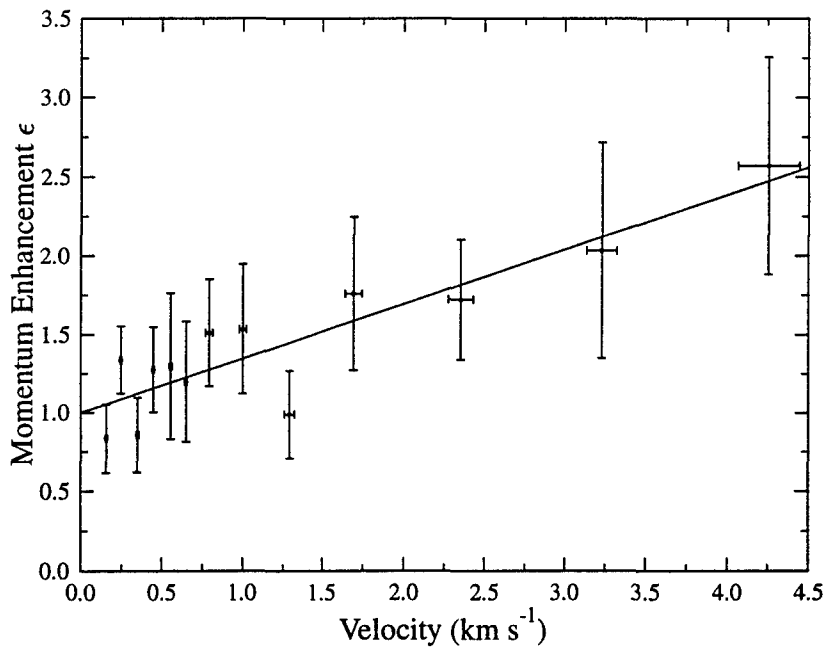

Figure 9. Momentum enhancement for iron microparticle impacts on Zagami meteorite. Error bars are the standard deviation of the binned data.

Summary

The momentum enhancement results are summarised in the following table:

Target	Function	Enhancement at 1 km s^{-1}	Enhancement at 4.5 km s^{-1}
Metal	$\mathcal{E} = 1+0.2(v-1.5)$	1	1.6
Meteorite	$\mathcal{E} = 1+0.35v$	1.35	2.6

3.2. Secondary Impact Plasma

3.2.1. Theory

When the ejecta from a primary impact reimpacts on a secondary surface it will liberate plasma if the ejecta velocity is sufficiently great (typically > 1.5 kms^{-1}) in just the same way as plasma is liberated from the primary impact. Hence it is reasonable to assume a comparable dependence on mass and velocity of the form

$$Q = cm^{\alpha}v^{\beta} \tag{14}$$

where c, α and β are constants. α is close to, and is often assumed to be equal to, unity.

3.2.2. Results

The plasma yield from primary impacts of iron particles on rhodium, normalised to the mass of the impacting particle, is shown in Figure 10. The equation fitted to the data is

$$Q/m = 8.54 \times 10^{-3} \, v^{4.74} \tag{15}$$

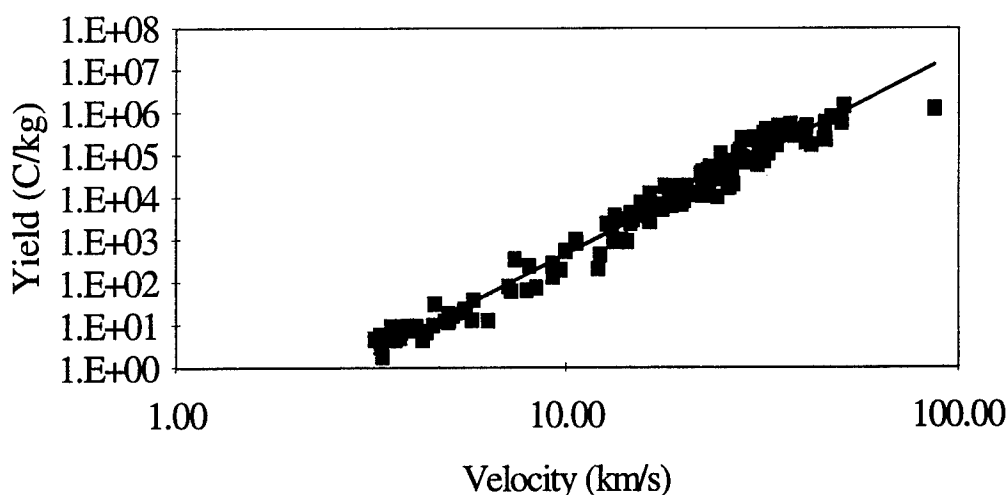with Q in Coulombs, m in kilograms and v in kms^{-1}.

Figure 10. Primary impact plasma yield for iron microparticle impacts on rhodium (from Ratcliff et al. 1995).

We will assume that this equation also applies to the yield from secondary impacts of the (primarily) rhodium ejecta on the (molybdenum) grid. Implications of this assumption are discussed below.

The yield of secondary plasma, again normalised with respect to mass of the primary projectile, is shown in Figure 11. Here the fit has been derived as

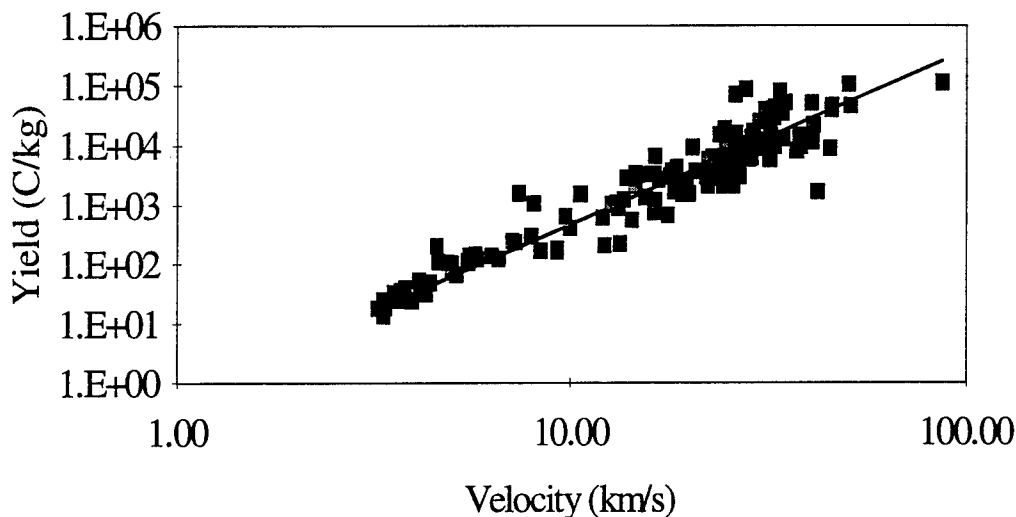$$Q/m = 0.570v^{2.916} \qquad (16)$$

Figure 11. Secondary impact plasma yield for iron microparticle impacts on rhodium (from Ratcliff et al. 1995).

Allowing for the 85% transparency of the grid resulting in only 15% of the ejecta being seen (the transparency of the grid is in fact weakly dependent on the ejecta trajectory, but the nominal figure will be used),

$$Q/m = 3.8v^{2.916} \qquad (17)$$

The dependence of the yield of secondary impact plasma on the velocity of the primary particle is thus much less than is the case for the primary impact plasma. It follows that at high impact velocities the total plasma yield is dominated by the primary impact plasma, while secondary plasma dominates at low velocities.

3.3. Ejecta Kinetic Energy

3.3.1.Theory
The functional dependence of momentum enhancement and secondary impact plasma production on the mass and velocity of the ejecta particles (equations 7 and 14) provide two simultaneous equations in m_e and v_e. Simultaneous measurements of the momentum enhancement and the ion yield from secondary impacts thus allow these equations to be solved for m_e and v_e. Assuming the distributions these two parameters represent can be expressed by 'characteristic' values, we can thus solve individually for

m_e and v_e and hence calculate the ejecta kinetic energy. We use the phrase 'characteristic' as these values will not represent true average or mean values in the conventional sense. However, an assumption intrinsic to this reasoning is that the ejecta produces both momentum enhancement and secondary impact plasma. This is reasonable in the case of a ductile target material where the ejecta is dominated by high speed material, but is not the case for a brittle material where the bulk of the mass is seen as low speed spallation ejecta which will not produce plasma when it re-impacts. While it is thus possible to derive the ejecta kinetic energy for the rhodium target, it is unfortunately not possible to do so for the Zagami meteorite sample.

Dividing equation 14 by $p_e = m_e v_e$ yields

$$v_e = \left(\frac{Q}{cp_e}\right)^{1-\beta} \tag{18}$$

and hence

$$m_e = \left(\frac{Q}{c}\right)^{\beta-1} p_e^{\,2-\beta} \tag{19}$$

giving

$$KE_e = \frac{1}{2}\left(\frac{Q}{c}\right)^{1-\beta} p_e^{\,\beta} \tag{20}$$

This provides an independent measurement which can be compared with the result derived from the momentum enhancement measurement alone. Each method involves making certain assumptions, but as these are different in each case a good correlation of the results implies a reliable measurement. Since momentum enhancement is only a measure of the perpendicular component of the ejecta velocity while secondary plasma production is insensitive to angle, one assumption that has to be made is the average trajectory (or the trajectory distribution). We use the values derived by Eichorn (1978) for iron impacts on gold, namely an average of 45° at 3.2 km s^{-1} impact velocity, 40° at 5.2 km s^{-1} and 30° at 7.9 km s^{-1}.

Although the ideal is to make as many measurements as possible simultaneously from each individual impact, in the present study separate experimental campaigns were performed to make the impact plasma measurements and the momentum enhancement measurements. The reason for this is that the momentum measurements were made using a piezoelectric (PZT) crystal electrically coupled to the target, while the plasma measurements involve collecting the negative impact plasma on the target and amplifying the signal. Since this collected charge would influence the response of the PZT, it was deemed advisable to perform the measurements separately.

3.3.2. Results
Using the formula for secondary ion yield derived above (equation 17) to calculate the yield that would have been expected for each of the momentum enhancement events,

the primary yield formula (equation 15) serves as the second simultaneous equation to derive the total ejecta mass and characteristic velocity, and hence the kinetic energy.

Calculating in the first instance the mass of ejecta per unit projectile mass we obtain the results shown in Figure 12. The top line is based on the assumption of a constant 45° average ejection angle, the middle line on Eichorn's data (Eichorn 1978) but assuming 30° applies also to high velocities, and the lowest curve uses an extrapolation of Eichorn's observed ejection angle trend with velocity.
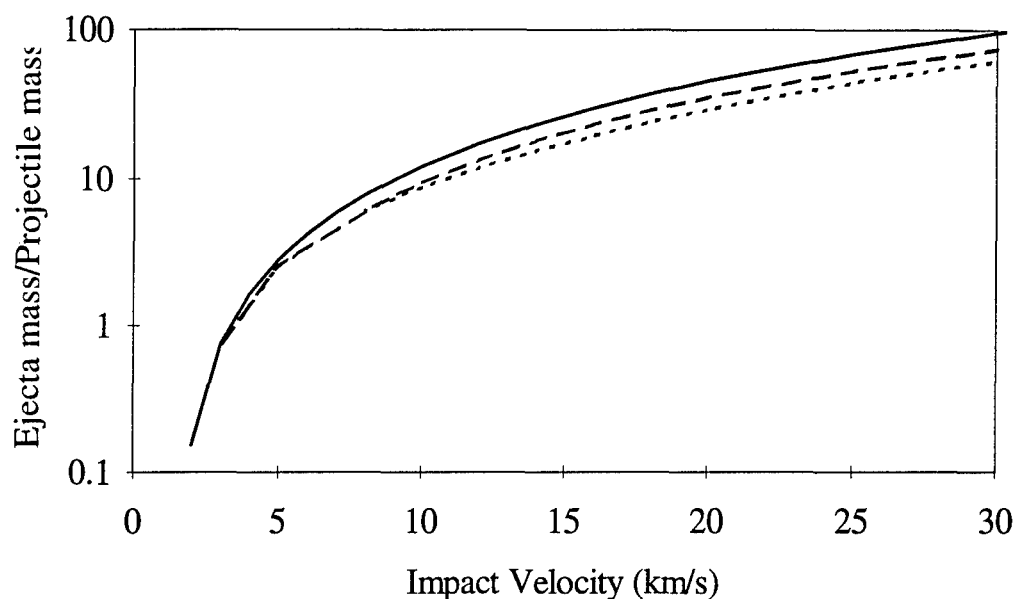

Figure 12. Calculated ejecta masses normalised with respect to projectile mass as a function of impact velocity. Solid line = 45° ejection angle invariant with velocity, dashed line = angle falls from 45° to 30° at 8 kms^{-1} but constant thereafter, dotted line = angle falls from 45° to zero (from Ratcliff et al. 1995).

We see zero ejecta mass below 1.5 km s^{-1} impact velocity, rising to equal projectile mass at ~3 km s^{-1} and, thereafter, ejecta must be dominated by target material as the ejecta mass greatly exceeds the projectile mass. The effect of the assumed variation in ejecta angular distribution is small.

Converting these ejecta masses into crater volumes (assuming hemispheric form), we can compare the results with those predicted by published cratering equations. Figure 13 shows a comparison of calculated crater diameter normalised with respect to projectile diameter as a function of impact velocity. Plotted for comparison are predictions based on the crater diameter equation of Watts et al. (1994) and on the foil penetration formula of McDonnell and Sullivan (1992) (assuming a ratio of 1.5 between foil thickness at the ballistic limit and equivalent semi-infinite target crater depth).

The two theoretical lines demonstrate the wide range that current predictive capability still allows. In view of this our derived values are reasonable. We would expect our

17

estimates to be lower than the true values as we do not allow for crater excavation by any means other than material ejection. Of significance in these comparisons, no account is taken of material compaction or plastic deformation which would enlarge crater volume without ejecta formation. We derive from our approach a zero crater volume for low velocity impact but there may well be such deformation.
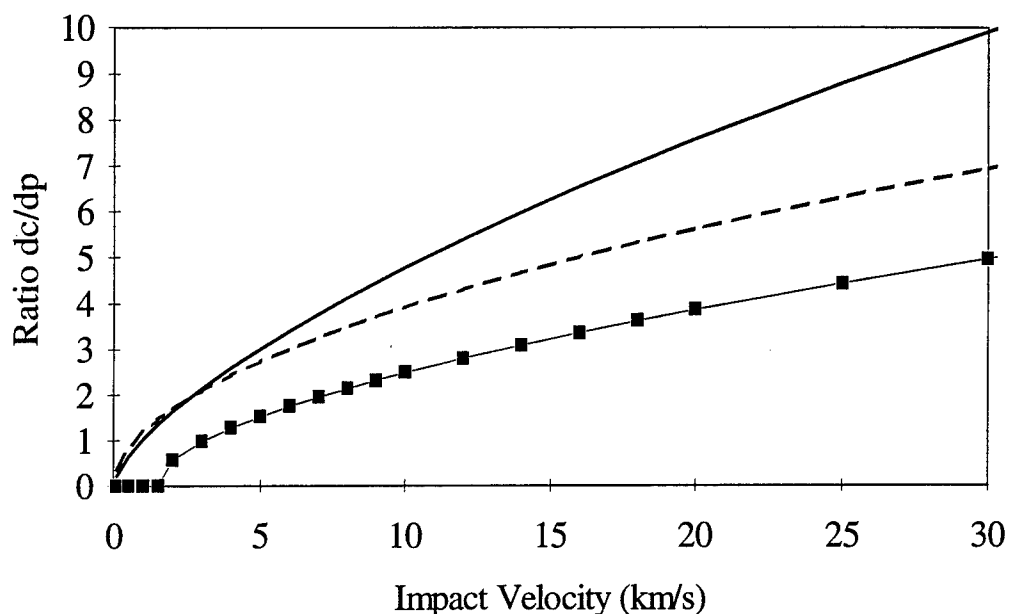

Figure 13. Calculated crater diameter, normalised with respect to the projectile diameter, based on experimental data (for constant 45° ejection angle) and two theoretical equations. Solid line = McDonnell and Sullivan (1992), dashed line=Watts et al. (1994) (from Ratcliff et al. 1995).

The ejecta masses derived above imply characteristic ejection velocities as shown in Figure 14.

The zero ejecta velocity for impact velocities below 1.5 km s^{-1} simply reflects the absence of ejecta. We then obtain a characteristic ejecta velocity of around 2 km s^{-1} with only a relatively weak dependence on the impact velocity. This is to be expected. While the maximum ejecta velocity would be expected to rise with increasing impact velocity, the minimum ejecta velocity occurs when the shock wave strength only slightly exceeds the strength of the material. For any impact velocity we thus expect to see low velocity ejecta and its presence moderates the dependence of the characteristic velocity on the impact velocity. Again the dependence on the assumed angular distribution of ejecta is weak.

The implication of the derived ejecta masses and velocities for the ejecta kinetic energies are shown in Figure 15. The ejecta kinetic energy is expressed as a percentage of the incident particle kinetic energy as a function of impact velocity.
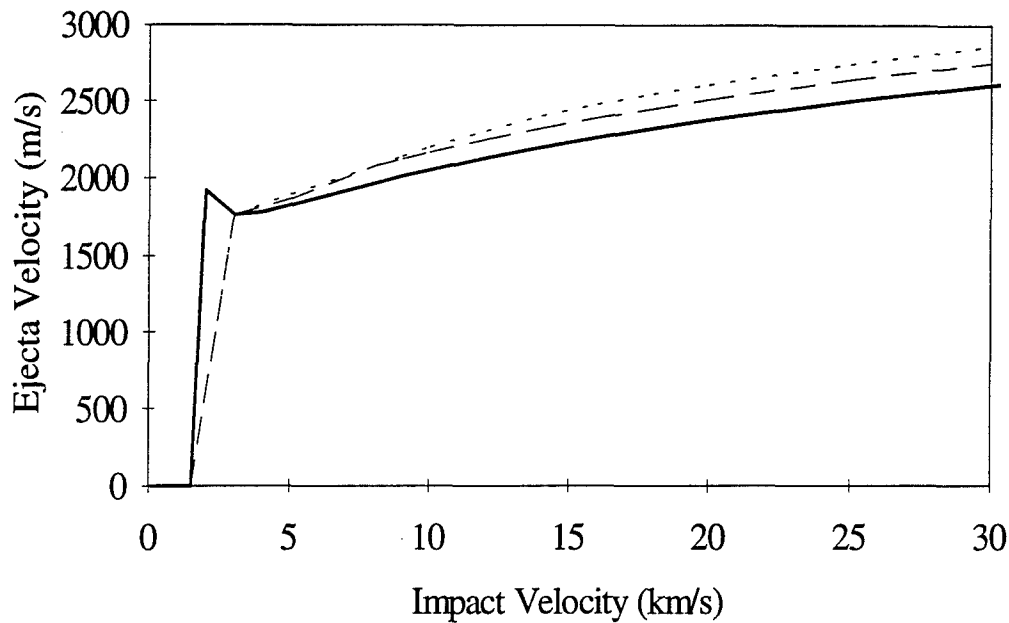
Figure 14. Derived characteristic ejecta velocities vs impact velocity. Solid line = 45° ejection angle invariant with velocity, dashed line = angle falls from 45° to 30° at 8 km s^{-1} but constant thereafter, dotted line = angle falls from 45° to zero. The apparent difference below 3 km s^{-1} is due to the absence of a 2 km s^{-1} datum in the latter two data sets. (From Ratcliff et al. 1995).

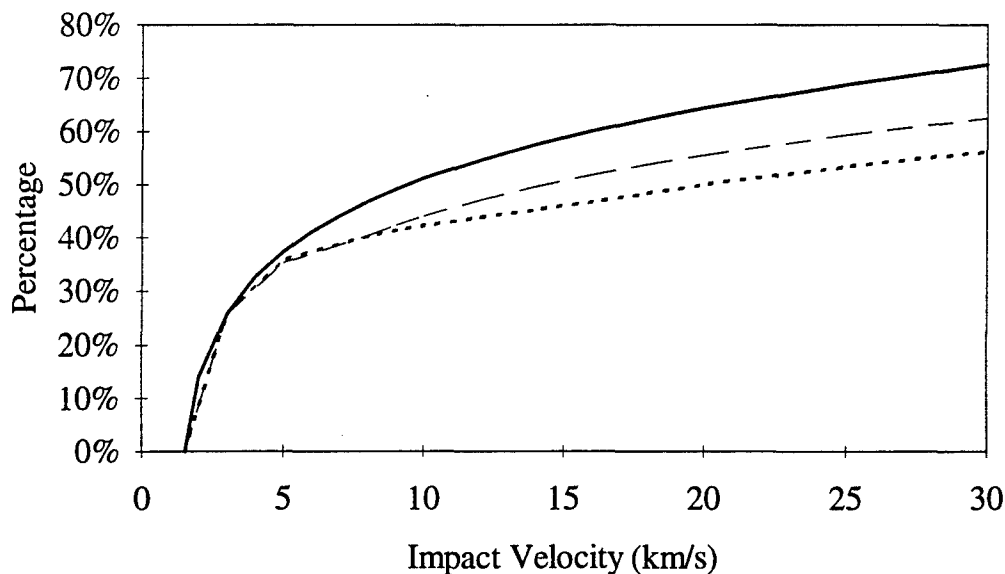Figure 15. Partitioning of the projectile kinetic energy to ejecta kinetic energy as a function of impact velocity. Solid line = 45° ejection angle invariant with velocity, dashed line = angle falls from 45° to 30° at 8 km s^{-1} but constant thereafter, dotted line = angle falls from 45° to zero. (From Ratcliff et al. 1995).

19

Again we see that the influence of the assumed ejecta angular distribution is weak. The percentage of the projectile kinetic energy converted to ejecta kinetic energy rises rapidly when the threshold velocity of 1.5 km s^{-1} is exceeded and flattens off at higher velocity. This form is palpably correct - the value must be zero at low velocities where no ejecta is produced and can not exceed 100% at any velocity. However, the absolute values require some further consideration.

Firstly, when applied to secondary plasma production the 'm' in equation 14 is not strictly the total ejecta mass, but only the integrated mass with velocity greater than the critical threshold velocity for plasma production (~1.5 km s^{-1}). It is well known that for brittle target materials the majority of the ejecta mass is seen to be low velocity spallation (e.g. Frisch 1992), but as a ductile material this will not be the case for rhodium. Eichorn (1978) measured ejecta velocities for iron particle impacts on gold (a system more comparable to ours) for impact velocities of 3 to 8 km s^{-1} and found none below ~1.5 km s^{-1}. However, his detection technique was based on the light emitted on impact and so suffers from a similar velocity threshold selection effect. If the mass in equation 14 is significantly lower than the total ejecta mass, equation 20 tells us that we will have overestimated the ejecta kinetic energy.

Secondly we have to address the question of whether the constants in equation 14 derived for the primary impact apply to the secondary plasma yield. In particular the primary equation was derived for particles with a minimum size of 28 nm whereas secondary plasma is produced by particles with a range of sizes down to single atoms and ions. The inaccuracy introduced by the different materials involved in the primary and secondary impacts will be small as ion yields do not vary greatly for any metal-on-metal impact. The fact that the ejecta will be 'hot' will have an influence which can not be quantified at this stage. Ion yield experiments with heated targets can be performed to address this question. If this effect is significant it will result in an underestimate of the ejecta kinetic energy, opposing the mass velocity threshold factor described above.

There is little or no published data directly comparable with our results. Gault and Heitowit (1963) measured energy partitioning for aluminium impact in basalt at 6.25 km s^{-1} and obtained values of 43-53% for ejecta kinetic energy. Our value at 6.25 km s^{-1} is 36-41% depending on the assumed ejecta trajectory distribution. Since metals are ductile one would expect reduced ejecta production (particularly through spallation) and increased plastic deformation compared with brittle materials such as basalt, and so our results appear highly credible.

The technique is open to further refinement. Ejecta trajectory distributions, once defined by independent measurement, can be used instead of the assumed average ejection angles. This will have only a small effect on the results, but by removing one of the unknown parameters will allow the ejecta velocity distribution to be derived from the time-profile of the secondary plasma signal. This distribution can then be used instead of the assumed 'characteristic' velocity.

The major remaining 'unknown' is the effect of the elevated temperature of the ejecta on the secondary plasma yield. Experiments could be performed using heated targets to quantify the uncertainty that this effect will have on the results. However, in order to include the effect in the analysis involves including a fourth variable (temperature) in

the characterisation of ejecta (in addition to mass, velocity and trajectory). Measurement of ejecta temperature (through time and spatially resolved light emission) is feasible, but falls beyond the scope of this work.

4. HYDROCODE SIMULATIONS

4.1. Purpose and Requirements

The primary purpose of hydrocode simulations is to allow the parameter space (mass, velocity, materials) of the experimental measurements to be extended beyond the range of the experimental facilities. The first step in this process is to reproduce actual experimental results in order to establish confidence in the simulations.

Simulations have been performed using the hydrocode Autodyn 2D (marketted by Century Dynamics Inc.) implemented on a 66 MHz 486 PC. The processor and memory limitations allow normal incidence impact problems to be simulated using 2D axial symmetry with a mesh resolution (at the impact site) of 0.05 μm. With a standard simulated particle dimension of 1 μm, this provides 20 cells across one particle diameter. The Johnson-Cook material model (Johnson and Cook 1983) (incorporating work hardening and strain and strain rate softening of material) is used in conjunction with the Tillotson equation of state. This is implemented in its original two-phase solid-gas form (Tillotson 1962).

Simulations have also been performed using CTH, with the help of David Medina of the US Air Force Phillips Laboratories. The anticipated collaboration with Dr. E. Hertel at the Sandia Laboratories, aimed at using CTH simulations to derive momentum enhancement results, was not realised due to new commitments taken on by our colleague.

In view of the emphasis of the research programme on characterising the kinetic energy of ejecta for impacts on either spacecraft or astrophysical material, emphasis was placed on attempting to produce realistic simulations of ejecta. Hydrocodes are known to be capable of producing good simulations of the debris clouds produced by the penetration of plates, but there have been few or no investigations of ejecta from impacts on semi-infinite targets published.

4.2. Autodyn

Autodyn incorporates three possible calculation schemes, Lagrangian, Eulerian and ALE (Arbitrary Lagrangian-Eulerian). Neither the Lagrangian nor the ALE processor allow ejecta to be produced by impacts on semi-infinite targets. The Lagrangian processor accommodates large distorions in the grid by use of an erosion algorithm which discards material from the calculation when the strain exceeds a definable value - this results in material being eroded before it can be ejected. The ALE processor, by imposing a Lagrangian surface on an Eulerian interior, requires continuity of the material surface.

The Eulerian processor does allow for ejecta production. However, the results obtained were disappointing as too little ejecta is produced. The ejecta kinetic energy can, in principle, be derived by two methods. The simplest is to use the code's energy-tracking capability to measure the kinetic energy at a very late stage of the calculation after the crater has frozen and motion of the target has damped out. However, at these extremely late stages the accumulated error in the energy conservation exceeds the kinetic energy of the ejecta. The alternative method is to examine the kinetic energy of each cell of ejected material individually. This produces a more reliable value but one which only reflects the failing in ejecta production. Discussion with technical experts at Century Dynamics Inc. attributed this failing to the fact that at present Autodyn only incorporates a 1st order Eulerian processor. The 2nd order Eulerian processor or the Smooth Particle Hydrodynamics processor in development are believed to be capable of better simulation accuracy. However, neither were available during the period of this research programme.

4.3. CTH

The CTH hydrocode, by virtue of being a 2nd order Eulerian code, should produce better results than Autodyn. Unfortunately the use of the Phillips Labs computers for classified work limited UKC access to CTH. A number of runs were performed by David Medina to UKC specification. These deomonstrated that CTH momentum and energy tracking provided sufficient accuracy to give meaningful results, while visual inspection of the material location plots suggested more realistic ejecta distributions than were produced by Autodyn. Unfortunately the mechanism for deriving the momentum and kinetic energy of the ejecta itself (as apposed to the material sum) had not been established by the end of the research programme.

5. PARAMETRIC EQUATIONS

In order to provide a means of predicting energy partitioning as a function of target and projectile parameters it is necessary to derive parametric equations. This has been done using the experimental results derived in this research programme and those from the previous programme (USAF/EOARD Contract F49620-93-1-0487). It has been possible to derive results in terms of the dependence of partitioning of energy to various routes on the mass and velocity of the projectile for iron particles impacting metallic targets. However, as yet there is not enough data to include material properties of the projectile or target, although some general conclusions can be drawn concerning differences between different types of target material (i.e. ductile vs brittle).

5.1. Momentum enhancement

The data reported here, coupled with that of Stradling et al. (1990), Rembor (1993) and Slattery and Roy (1970), suggest that momentum enhancement for iron particle

impacts on metallic (i.e. ductile) targets shows little dependence on the target material, and has the form:

$$\mathcal{E} = 1 \qquad \text{for } v < 1.5 \text{ km s}^{-1} \qquad (21)$$

$$\mathcal{E} = 1 + 0.2(v-1.5) \qquad \text{for } v > 1.5 \text{ km s}^{-1} \qquad (22)$$

For brittle materials (represented by our results for impact on Zagami meteorite) the velocity-dependence is stronger and no threshold is seen:

$$\mathcal{E} = 1 + 0.3v \qquad (23)$$

In each case the velocity range over which these results have been derived is ~0 - 5 km s^{-1}, though the range can be extrapolated with a reasonable degree of confidence to perhaps 10 - 20 km s^{-1}.

5.2. Light Emission

The energy of electromagnetic radiation emitted at visible wavelengths for iron microparticle impacts on rhodium has been derived by Burchell (1994), from which it is derived that the partitioning of energy to visible light emission is given by:

$$\frac{E_{em}}{KE_p} = 4.6 \times 10^{-7} v^2 \qquad (24)$$

for v measured in km s^{-1}. Burchell et al. (1996b) report that the energy in the the light flash measured from iron microparticle impacts on ice is a factor of 4.6 lower than that for metallic targets. These results are based on data up to velocities up to ~70 km s^{-1} and can thus be assumed to be applicable to essentially all space impacts except those involving interstellar particles.

5.3. Ionisation

The fraction of impactor energy seen in the kinetic energy of impact plasma ions and used in ionising those ions was given in graphic form in the final report of USAF/EOARD Contract F49620-93-1-0487 (Ratcliff 1994). Parameterising those results yields:

Ionisation: $\qquad\qquad \dfrac{E_i}{KE_p} = 3.0 \times 10^{-6} v^{1.7} \qquad (25)$

Ion kinetic energy: $\qquad \dfrac{KE_{ions}}{KE_p} = 4.9 \times 10^{-6} v^{1.9} \qquad (26)$

Total: $\qquad\qquad\qquad \dfrac{E_{ions}}{KE_p} = 8.1 \times 10^{-6} v^{1.8} \qquad (27)$

These results are based on experimental data up to ~80 km s^{-1} and are thus also valid throughout the impact velocity range of significance for space impacts, with the exception of interstellar velocities.

5.4. Ejecta Kinetic Energy

Fitting an equation of the form F = 1 - a*(v-0.5)$^\beta$ (F is the fraction of the incident particle kinetic energy and a, b and β are constants) to the results shown in Figure 15 for iron impacts on rhodium gives the result

$$F = 1 - 0.977(v-0.5)^{-0.228} \qquad \text{for } v > 1.5 \text{ km s}^{-1} \qquad (28)$$

with a correlation of 97.86%. However, simplifying the fit to the form

$$F = 1 - \frac{1}{\sqrt[4]{(v-0.5)}} \qquad \text{for } v > 1.5 \text{ km s}^{-1} \qquad (29)$$

only reduces the correlation to 96.94%. The constant 0.5 ensures that F = 0 at v = 1.5 km s^{-1}, thus giving the observed velocity threshold. In view of the precision of the measurements on which this is derived, and on the basis of the small dependence of momentum enhancement and impact ionisation measurements on the type of metallic target, this equation provides a useful basis for estimating ejecta kinetic energy for such target materials.

These results are based on a combination of the momentum enhancement and impact plasma data, and thus have a strict validity range of 0 - 5 km s^{-1}, with a reasonable degree of confidence possible for extrapolation to 10 - 20 km s^{-1}.

The kinetic energy of the liberated ions is a constituent of the total kinetic energy, so the kinetic energy of solid, liquid and vapour ejecta is the difference between the total kinetic energy and that of the plasma. At all velocities this is over two orders of magnitude greater than the kinetic energy of the ions.

5.5. Other Paths

The energy dissipated through other paths (acoustic waves, comminution, plastic deformation etc) is the difference between the kinetic energy of the impactor and the sum of the energy dissipated in the identified paths.
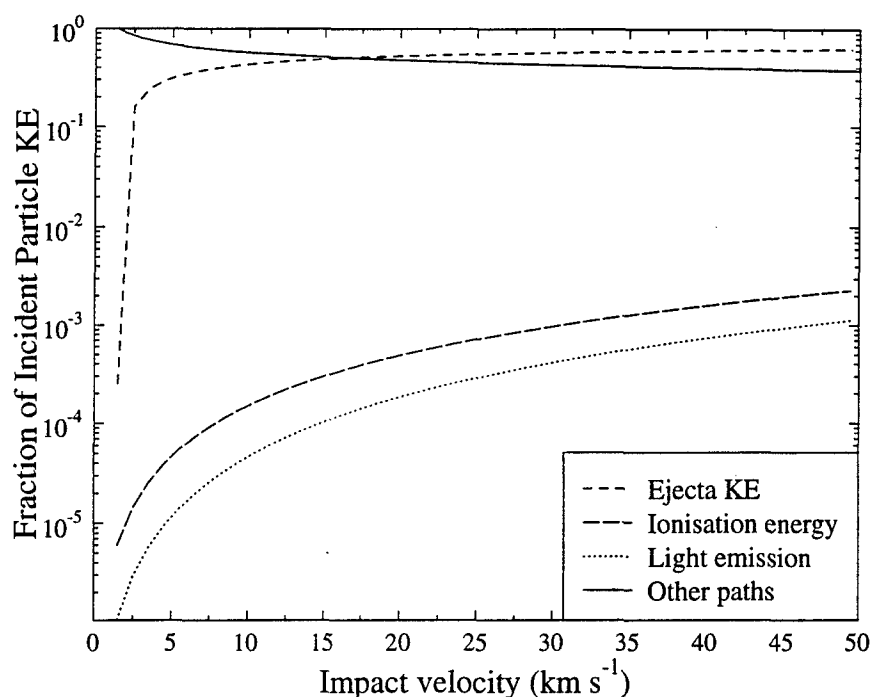
Figure 15. Energy partitioning for impacts of iron microparticles on metallic targets.

6. FURTHER WORK

We have seen the real progress towards defining energy and momentum partitioning relationships from the current work, at velocities well in excess of those achieved elsewhere on the international scene. The work would benefit from an extended investigation of material dependencies in the impact processes, from enhancements in the velocity at which momentum enhancement measurements can be made (cooled PZT sensor and/or amplifier, improved particle charging in the accelerator) and from measurements of the angular distribution of ejecta.

We identify two particular areas of collaboration highly pertinent for joint development:

1) Planetary Defence.
Experimentation and parameter characterisation on a range of 'astrophysical surfaces' relevent to planetary defence. Although we have performed the first momentum exchange measurements on meteoritic material, this is for a flat semi-polished surface. Representative space-eroded surfaces and regoliths could be mimiced with these meteorites to yield more realistic reactions of a NEO to energy exchange at interception in space. This scenario and issues of effectiveness at macroscale depend on the same physics we have investigated at microscale.

25

2) Secondary Momentum Measurement

Kent has developed techniques for 'secondary' measurement of momentum exchange, namely the ejecta momentum which can be measured directly and hence resolved spatially to give greater depth in the understanding of the detail of momentum exchange; the characteristic ejecta mass and velocity used (albeit effectively) in this report can be replaced by a higher order distribution of ejecta velocity and mass, and further - the angular distribution used.

REFERENCES

M.J. Burchell, 'Design of an Impact Diagnostic Chamber to Study Energy Partitioning in a Time and Spatially Resolved Manner', in: J.A.M. McDonnell, Investigation of Optical Damage, Energy Partitioning and Scaling Laws at Extremely High Velocities, Final Report of Contract F49620-93-1-0487, University of Kent (1994).

M.J. Burchell, L. Kay and P.R. Ratcliff, 'Use of Combined Light Flash and Plasma Measurements to Study Hypervelocity Impact Processes', Adv. Space Res. Vol. 17 No. 12, pp. (12)141-(12)145 (1996a).

M.J. Burchell, M.J. Cole and P.R. Ratcliff, 'Light Flash and Ionization from Hypervelocity Impacts on Ice', Icarus, in press.

E.L. Christiansen, E. Cykowski and J. Ortega, 'Highly Oblique Impacts into Thick and Thin Targets', Int. J. Impact Engng 14, pp. 157-168 (1993).

S.K. Croft, 'Hypervelocity Impact Craters in Icy Media', Lunar Planet. Sci. XII, pp. 190-192, (1981).

G. Eichorn, 'Primary Velocity Dependence of Impact Ejecta Parameters', Planet. Space Sci. 26, pp. 469-471 (1978).

G. Eichorn and E. Grün, 'High Velocity Impacts of Dust Particles in Low-Temperature Water Ice', Planet. Space Sci. 41, pp. 429-433 (1993).

W. Frisch, 'Hypervelocity Impact Experiments with Water Ice Targets', in: Hypervelocity Impacts in Space. ed. J.A.M. McDonnell, University of Kent at Canterbury, pp. 7-14, (1992).

D.E. Gault and E.D. Heitowit, Proc. Symp. Hypervel. Impact 6th 2, pp. 419-456, (1963).

C.J. Hayhurst, H.J. Ranson, D.J. Gardner and N.K. Birnbaum, 'Modelling of Microparticle Hypervelocity Oblique Impacts on Thick Targets', presented at the Hypervelocity Impact Symposium, Santa Fe, New Mexico, 17-19 October, 1994.

G.R. Johnson and W.H. Cook, 'A Constitutive Model and Data for Metals Subjected to Large Strains, High Strain Rates and High Temperatures', Proc. 7th Int. Symp. on Ballistics, The Hague, The Netherlands, (1983).

J.A.M. McDonnell, D.J. Gardner, P.J. Newman, N.J. Robertson and C.J. Hayhurst, 'Hydrocode Modelling in the Study of Space Debris Impact Crater Morphology', Proc. 1st European Conf. on Space Debris, Darmstadt, Germany, pp. 425-432 (1993).

J.A.M. McDonnell and K. Sullivan, 'Hypervelocity Impacts on Space Detectors: Decoding the Projectile Parameters', in: Hypervelocity Impacts in Space, ed. J.A.M. McDonnell, University of Kent at Canterbury, pp. 39-47, (1992).

N.G. Mackay, S.F. Green, D.J. Gardner and J.A.M. McDonnell, 'Experimental Investigation of the Relationship Between Impact Crater Morphology and Impacting Particle Velocity and Direction', 3rd LDEF Post-Retrieval Symp., Williamsburg, 1993.

P.R. Ratcliff, 'Energy Partitioning in Hypervelocity Impacts, in: J.A.M. McDonnell, Investigation of Optical Damage, Energy Partitioning and Scaling Laws at Extremely High Velocities', Final Report of Contract F49620-93-1-0487, University of Kent (1994).

P.R. Ratcliff, J.A.M. McDonnell, J.G. Firth and E. Grün, 'The Cosmic Dust Analyser', J. Brit. Interplanetary Soc. 45 No. 9, pp. 375-380, (1992).

P.R. Ratcliff, M.J. Cole, J.A.M. McDonnell, H.A. Shaw and F. Allahdadi, 'Experimental Determination of Energy Partitioning in Microparticle Impacts at

Velocities from 1 to 100 kms⁻¹', paper IAF-95-I.5.03, presented at the 46th International Astronautical Congress, October 2-6, 1995, Oslo, Norway.

P.R. Ratcliff, F. Gogu, E. Grün and R. Srama, Plasma production by secondary impacts: implications for velocity measurements by in-situ dust detectors, *Adv. Space Res.* **17**(12), 111-115 (1996a).

P.R. Ratcliff, M.J. Burchell, M.J. Cole, T.W. Murphy and F. Allahdadi, 'Experimental Measurements of Hypervelocity Impact Plasma Yield and Energetics', *Int. J. Impact Engng* (in press), and to be presented at HVIS '96, Freiberg, Germany.

K.M. Rembor, 'Momentum Exchange at Particle Impacts - A Calibration Study for the Giotto/DIDSY Momentum Sensors', Diploma Thesis, University of Kent at Canterbury, 1993.

J.C. Slattery and N.L. Roy, 'Investigations of Hypervelocity Impact Phenomena', NASA CR-66872 or Report 11489-6012-RO-OO, TRW Systems Group, Redondo Beach, CA, (1970).

G.L. Stradling, G.D. Idzorek, P.W. Keaton, J.K. Studebaker, A.A. Hopkins Blossom, M.T. Collopy, H.L. Curling Jr. and S.D. Bergeson, 'Searching for Momentum Enhancement in Hypervelocity Impacts', Int. J. Impact Engng **10**, pp. 555-570, (1990).

J.H. Tillotson, 'Metallic Equations of State for Hypervelocity Impact', General Atomic Report AG-3612, San Diego, (1962).

J.M. Thomsen, M.G. Austin and P.H. Schultz, Lunar Planet. Sci. **XI**, pp. 1146-1148, (1980).

A.J. Watts and D. Atkinson, 'Dimensional Scaling for Impact Cratering and Perforation', presented at the Hypervelocity Impact Symposium, Santa Fe, New Mexico, 17-19 October, 1994.

7. APPENDICES

P.R. Ratcliff, M.J. Cole, J.A.M. McDonnell, H.A. Shaw and F. Allahdadi, 'Experimental Determination of Energy Partitioning in Microparticle Impacts at Velocities from 1 to 100 kms^{-1}', paper IAF-95-I.5.03, presented at the 46th International Astronautical Congress, October 2-6, 1995, Oslo, Norway.

P.R. Ratcliff, M.J. Burchell, M.J. Cole, T.W. Murphy and F. Allahdadi, 'Experimental Measurements of Hypervelocity Impact Plasma Yield and Energetics', *Int. J. Impact Engng* (in press), and to be presented at HVIS '96, Freiberg, Germany.

IAF-95-I.5.03

Experimental Determination of Energy Partitioning in Microparticle Impacts at Velocities from 1 to 100 kms^{-1}

P.R. Ratcliff. M.J. Cole. J.A.M. McDonnell and H.A. Shaw
Unit for Space Sciences. Physics Department. University of Kent at
Canterbury, Canterbury, Kent. CT2 7NR. UK

F. Allahdadi
US Air Force. Space Kinetic Impact and Debris Branch. PL/WSCD. Phillips
Laboratories. Kirtland AFB. Albuquerque. NM 87117. USA

46th International Astronautical Congress
October 2-6, 1995/ Oslo, Norway

EXPERIMENTAL DETERMINATION OF ENERGY PARTITIONING IN MICROPARTICLE IMPACTS AT VELOCITIES FROM 1 TO 100 kms^{-1}

P.R. Ratcliff, M.J. Cole, J.A.M. McDonnell and H.A. Shaw
Unit for Space Sciences, Physics Department, University of Kent at Canterbury, Canterbury, Kent, CT2 7NR, U.K.

F. Allahdadi
US Air Force, Space Kinetic Impact and Debris Branch, PL/WSCD, Phillips Laboratories, Kirtland AFB, Albuquerque NM 87117, USA.

Abstract

In a hypervelocity impact event the onset of all physical processes (e.g. impact plasma emission and the coupling of the magnetic field within it, impact flash, crater size and morphology and emission of ejecta) depend entirely on the way the total kinetic energy of the impactor is coupled and partitioned into the target. Of critical importance to spacecraft applications (primary damage and debris propagation) is the partitioning to ejecta kinetic energy. Experimental measurements have been made of the kinetic energy of ejecta (and the integrated mass and average velocity) generated by the impact of iron particles on rhodium. We find a threshold velocity for ejecta production at 1.5 ± 0.2 kms^{-1}. The ejecta kinetic energy partitioning then rises rapidly to ~40% at 8 kms^{-1}, and then more slowly to ~56% at 30 kms^{-1}. Extrapolation to 100 kms^{-1} yields a value of ~78%. The values at low velocity are low compared with those for brittle materials due to the greater relative partitioning to other routes.

Symbols

c	numeric constant
E_d	'decomposition' energy
m	mass
KE	kinetic energy
p	momentum
Q	ion yield
v	velocity
V	volume
α	numeric constant
β	numeric constant
ε	specific 'decomposition' energy
$\mathcal{E}$	momentum enhancement
θ	angle measured relative to the target normal
ρ	density

Subscripts

c	crater
e	ejecta
o	threshold
p	projectile
t	target
total	total

Introduction

Spacecraft operating in Earth orbit are subject to potentially damaging impact by both natural (micrometeorite) and man-made (space debris) origin. The hazard posed by such events depends on both the collision probability and the damage potential of impacts as a function of the impactor dynamic and material properties. An orbital object of ~1 cm diameter (or an interplanetary particle of higher velocity and

correspondingly smaller size) will have enough kinetic energy to cause catastrophic damage with a high probability. However, the damage potential is not limited to a consideration of the penetration and physical damage capability of the primary impact but also includes the capacity for production of plasma which may interfere with spacecraft operation[1] and of ejecta which may either reimpact on the primary target due to re-entrant geometry, or be emitted and add to the debris population thus increasing the future collision probability. This increases the potential lethality of impact by smaller objects.

Historically, the major source of orbital debris has been explosion of upper stages and satellites. In the future, with improved reliability of systems but also increased utilisation of space and of debris populations, the major cause is expected to be collision. The propagation of debris from an impact (whether in the 'forward' direction into the spacecraft following penetration of the skin or 'rearward' into free space) depends on the kinetic energy of the debris particles. Calculation and/or measurement of the partitioning of the incident particle kinetic energy to ejecta kinetic energy is thus critical to both damage prediction and debris propagation simulations.

The published literature contains details of some measurements of ejecta energies[e.g.2]. The motivation for much of this work has been planetary science and so the materials used have been geological rather than representative of spacecraft materials. The measurement technique has been typically via high speed photography of debris clouds produced from light gas gun impacts. The work presented here concerns an experimental method for measuring ejecta kinetic energy (via measurements of impact momentum enhancement and secondary plasma yield) using the 2MV Van de Graaff dust accelerator facility at the University of Kent at Canterbury. This facility, unlike light gas guns, can access the full range of velocities relevant to spacecraft applications, and by provision of a high count rate (several impacts per minute) coupled with real-time data acquisition and analysis allows large amounts of data to be collected and analysed on a statistical basis.

The work programme represents a collaboration between the Unit for Space Sciences at the University of Kent at Canterbury and the PL/WSCD division of the US Air Force, whose primary expertise is in computational predictive analysis of spacecraft survivability and vulnerability to kinetic impact.

Method

Momentum Enhancement

During a hypervelocity impact event an impact crater is typically formed, resulting from the ejection of target material from the impact site. If the impact occurs on a semi-infinite target, this ejecta (which will generally also contain material from the projectile) will have a net momentum component in the direction of the target normal, and so conservation of momentum dictates that an equal and opposite momentum is imparted to the target. If a momentum sensor is used on the target and has a response time which is long compared with the timescale of ejecta formation, the signal it records will be the sum of the incident particle and the ejecta momenta. Thus:

$$p_{total} = p_p + p_e = p_p(1 + p_e/p_p) = \mathcal{E}p_p \quad (1)$$

2

where $\mathcal{E}$ is defined as the momentum enhancement. For non-normal particle incidence the momenta are represented by vectors and $\mathcal{E}$ is represented by a diagonal matrix whose leading diagonal elements describe the enhancement in the direction of the target normal and in two perpendicular directions in the target plane. However, for normal incidence impacts, as was the case in this work, it is reasonable to assume that the debris cloud is radially symmetrical about the target normal and so there will be no net momentum parallel to the target plane. Momenta and $\mathcal{E}$ can thus be considered as scalar.

If we consider the two-dimensional distribution of the ejecta cloud then (regarding the impact site as a point source of ejecta) the mass ejected at angle θ is $m_e(\theta)d\theta$ and the component of the momentum in the direction of the target normal is

$$p_e(\theta) = m_e(\theta)d\theta v_e(\theta)\cos\theta \qquad (2)$$

where $v_e(\theta)$ is the mean ejecta velocity in direction θ.

Integrating over all ejection angles

$$p_e = \int_0^{\pi/2} m_e(\theta)v_e(\theta)\cos\theta d\theta \qquad (3)$$

and hence

$$\mathcal{E} = 1 + \frac{\displaystyle\int_0^{\pi/2} m_e(\theta)v_e(\theta)\cos(\theta)d\theta}{p_p} \qquad (4)$$

We can apply constraints to the velocity of the ejecta since conservation of energy

demands that the mean velocity of the material ejected into angular segment $d\theta$ satisfies the equation

$$\frac{1}{2}\int_0^{\pi/2} m_e(\theta)d\theta \left(\int_0^{\pi/2} v_e(\theta)d\theta\right)^2 = \frac{1}{2}m_p v_p^2 - E_d$$

$$(5)$$

E_d is the fraction of the incident particle kinetic energy that is not transferred to ejecta kinetic energy. This includes energy 'lost' to material heating, compaction, fragmentation etc., and is loosely referred to as the 'decomposition energy'.

In order to proceed further we must define explicit expressions for $m_e(\theta)$, $v_e(\theta)$ and E_d. For high impact velocities and correspondingly large (with respect to the projectile size) craters the ejecta is dominated by target material and so the volume of ejecta can be approximated by the volume of the crater. This can be estimated using any of the empirical equations in the published literature[e.g.3]. This defines the mass integrated over θ, but the angular dependence is also significant as this affects the relative magnitudes of the ejecta momentum components normal to and parallel to the plane of the target. Attempts have been made to characterise this dependence, and the angular dependence of v_e, experimentally for a variety of projectile and target materials[e.g.2,4,5,6], and the results of Eichorn[4] (the only study using metal targets) will be used in the analysis below. If assumptions are made about the angular dependence of m_e and v_e then a 'characteristic' ejecta velocity can be derived from the measurement of the ejecta momentum and the calculation of its mass, and so the ejecta kinetic energy can be estimated.

The assumption is frequently made in momentum enhancement work[e.g.7] that $v_e(\theta)$ and $m_e(\theta)$ are not velocity-dependent. This results in $\mathcal{E}$ being a linear function of impact velocity, though the assumption is not supported by experiment[e.g.4]. Generally the ejecta angular distribution tends towards the target normal with increasing impact velocity and so the normal component of the momentum is enhanced with respect to the radial component, resulting in an enhancement in momentum enhancement above linearity.

E_d is generally assumed to be proportional to the ejected mass of the target, i.e.

$$E_d = \varepsilon_t \rho_t V_c \qquad (6)$$

The constant of proportionality, ε_t, has the dimensions of specific energy and represents an 'effective decomposition energy'. However, if this assumption is adopted, along with the assumption that crater volumes are proportional to impactor kinetic energy[e.g.8], it follows that the ejecta kinetic energy represents a constant fraction (i.e. independent of impact velocity) of the impactor kinetic energy. This is obviously not the case, particularly at low impact velocities where little or no ejecta is generated. However, if the kinetic energy of the ejecta is measured by independent means, the 'decomposition energy' can be readily determined.

Secondary Impact Plasma

When the ejecta from a primary impact reimpacts on a secondary surface it will liberate plasma if the ejecta velocity is sufficiently great (typically > 1.5 kms^{-1}). The plasma yield from an impact has a characteristic dependence on mass and velocity of the form

$$Q = cm^{\alpha}v^{\beta} \qquad (7)$$

where c, α and β are constants. α is usually assumed to be equal to unity. Simultaneous measurements of the momentum enhancement and the ion yield from secondary impacts thus provide two simultaneous equations in m_e and v_e. Assuming the distributions these two parameters represent can be expressed by 'characteristic' values, we can thus solve individually for m_e and v_e and hence calculate the ejecta kinetic energy: dividing equation 7 by $p_e = m_e v_e$ yields

$$v_e = \left(\frac{Q}{cp_e}\right)^{1-\beta} \qquad (8)$$

and hence

$$m_e = \left(\frac{Q}{c}\right)^{\beta-1} p_e^{\,2-\beta} \qquad (9)$$

giving

$$KE_e = \frac{1}{2}\left(\frac{Q}{c}\right)^{1-\beta} p_e^{\,\beta} \qquad (10)$$

This provides an independent measurement which can be compared with the result derived from the momentum enhancement measurement alone. Each method involves making certain assumptions, but as these are different in each case a good correlation of the results implies a reliable measurement. Since momentum enhancement is only a measure of the perpendicular component of the ejecta velocity while secondary plasma production is insensitive to angle, one assumption that has to be made is the average trajectory (or the trajectory distribution). We use the values derived by Eichorn[4] for iron impacts on gold, namely an

4

average of 45° at 3.2 kms^{-1} impact velocity, 40° at 5.2 kms^{-1} and 30° at 7.9 kms^{-1}.

Although the ideal is to make as many measurements as possible simultaneously from each individual impact, in the present study separate experimental campaigns were performed to make the impact plasma measurements and the momentum enhancement measurements. The reason for this is that the momentum measurements were made using a piezoelectric (PZT) crystal electrically coupled to the target, while the plasma measurements involve collecting the negative impact plasma on the target and amplifying the signal. Since this collected charge would influence the response of the PZT, it was deemed advisable to perform the measurements separately until this effect could be reliably accounted for.

Accelerator Facility

The experiments described in this paper were performed on the 2 MV Van de Graaff dust accelerator at the University of Kent at Canterbury[9]. In this facility dust particles are charged (to ~10^{-13}-10^{-16} C) by contact with a needle mounted in the positive terminal of a Van de Graaff generator. They then fall down the potential well defined by field-grading rings along the flight tube. The kinetic energy of the particles is the product of their charge and the accelerating potential, so there is a strong correlation between the particle mass and the velocity achieved (see Figure 1). In-flight electrostatic detection of the particles provides a measure of their velocity and charge, and hence their mass can be calculated.

The accelerator can be used with a variety of dust materials. Iron and boron carbide are most commonly used, but various other metals, iron oxide, silver-coated glass and silicate are available. In this study all data has been taken using iron projectiles. The velocity range covered (0.4 to 87 kms^{-1}) corresponds to a mass range of 2x10^{-13} to 9x10^{-20} kg. The particles are spherical, so the corresponding size range is 3.6 μm to 28 nm diameter.
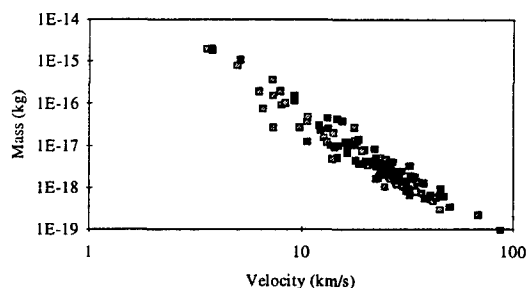

Figure 1. Mass-velocity data for the particles observed during the impact plasma measurement phase of this study.

Momentum Measurement Configuration

The experiment configuration for the impact momentum experiments is shown in Figure 2. A cylindrical piezoelectric crystal 5 mm in diameter and 10 mm long is mounted on a rigid surface using double-sided sticky tape. Electrodes have been deposited on each end of the cylinder. The front surface of the crystal is earthed, and the rear surface connected to a voltage amplifier. The crystal has a natural resonance frequency of 200 kHz and the amplifier and filters were matched to this to maximise the signal-to-noise ratio.

The impact target of rhodium foil is mounted (with bees wax) on the front surface of the crystal, and is also earthed. Although only 25 μm thick the foil still represents a semi-infinite target for the micron and submicron impact craters that are generated by the dust accelerator facility. Rhodium was used in this experiment as it is a well calibrated

material in impact plasma studies (it is the target material in the Chemical Analyser subsystem of the Cosmic Dust Analyser experiment on the Cassini/Huygens mission[10]), was available in high purity, and is relatively inert so the surface can be well characterised. Future experiments will be performed with materials more appropriate for spacecraft structure.
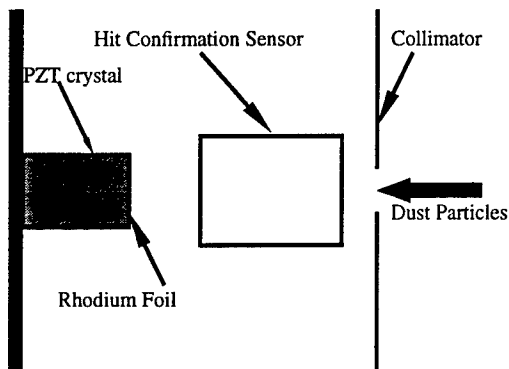

Figure 2. The experiment configuration for the impact momentum measurements.

Approximately 25 mm in front of the target a tube is mounted to allow electrostatic detection of incident particles to provide a 'hit confirmation' signal. Immediately in front of this tube is a collimating hole 2.5 mm in diameter which ensures that all events are limited to a confined range on the crystal. Even so, the sensitivity of the crystal is position-sensitive and so large numbers of events must be recorded and analysed statistically. The characteristics of the incident particle (velocity and charge, and hence mass) are measured by in-flight electrostatic sensors 'up stream' of the experiment.

Impact Plasma Measurement Configuration

The experiment configuration is shown in Figure 3. The target assembly was mounted in the small target chamber available at the impact facility. This has an internal diameter

of 30 cm, with 10 ports at 36° intervals around the side. The accelerator beam line was introduced to the chamber through one of these ports, and the particles allowed to impact on the target. The target itself consisted of a 25 μm thick rhodium foil bonded (with conductive epoxy resin) to a 0.5 mm thick aluminium plate, which was in turn mounted on a perspex block to provide electrical isolation. The target was maintained at a positive potential. A fine grid (150 lines per inch, 85% transparency) was mounted 3.3 mm in front of the target. This was electrically isolated from the target and was earthed. A planar electric field is thus sustained above the surface of the target, which separates the impact plasma.
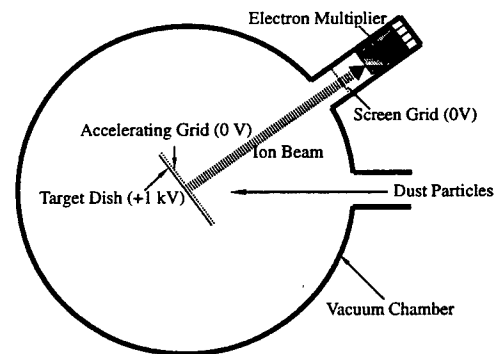

Figure 3. The experiment configuration for the impact plasma measurements.

The electrons (and any negative ions) are collected on the target (from which the signal is measured via a charge-sensitive amplifier) while the positive ions are accelerated in the direction of the target normal. In order to focus these ions on the electron multiplier, mounted in a tube attached to another of the chamber view ports, the target was mounted at an angle of 36° to the particle beam. This angle is not sufficient to cause elliptical craters to be produced[e.g. 11,12,13,14], and so one would still expect a symmetrical debris cloud thus maintaining the validity for comparison with the normal incidence momentum

measurements. The purpose of the electron multiplier was to allow time-of-flight mass spectrometric measurements of the impact plasma cloud. These results will be published in a future paper.

The waveforms recorded from the in-flight electrostatic particle detection, the target and the electron multiplier were recorded on a 4-channel digital storage oscilloscope and transferred to a PC for data archiving and analysis.

An obvious feature of the signals recorded from the target is that it consists of two components (Figure 4). The first component has a very fast risetime (~100-200 ns). Superimposed on this is a much slower signal with a risetime of several μs. The former represents the plasma from the primary impact. The risetime of this signal simply depends on the charge-to-mass ratio of the ions and the strength of the accelerating field. The latter represents ionisation liberated by the impact of ejecta from the primary event on the accelerating grid. The time-constant for this signal depends on the times-of-flight of the ejecta particles. (For a fuller explanation of signal shapes and formation see Ratcliff et al.[15]). The value of the accelerating field in these experiments was set to ensure that the two components of the signal were easily resolvable. Initially 1000 V was used. Subsequently two runs were performed using 500 V.

Results

Momentum Enhancement

A typical PZT waveform is shown in Figure 5. The crystal oscillates at its resonant frequency following excitation by the impact. The hit confirmation sensor and

particle in-flight sensor allow the time of impact to be identified on the PZT trace in order to confirm that the PZT signal corresponds to the impact of the measured particle. The signal level was derived by applying a digital smoothing filter to the waveform (the digitisation frequency of the oscilloscope was 100 MHz compared with the crystal frequency of 200 kHz), subtracting the baseline offset, squaring the waveform, picking off the peak value and square-rooting. The rms noise seen on the trace prior to the impact was subtracted from the signal in quadrature.
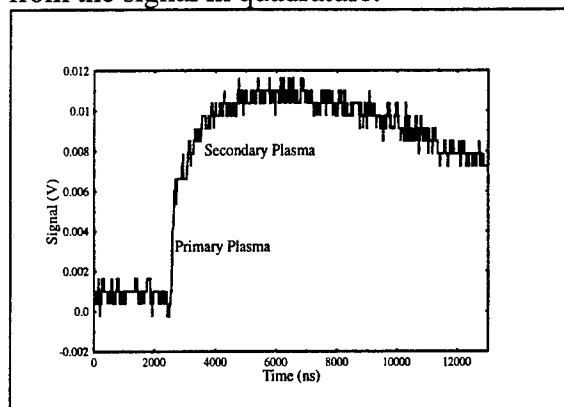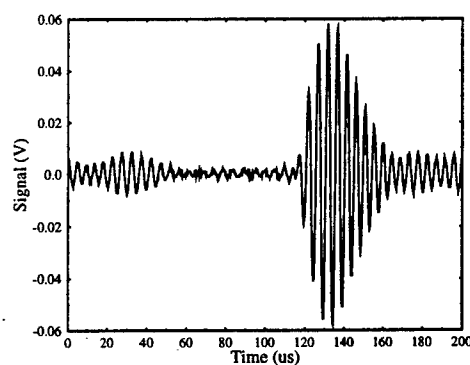

Figure 4. Typical target signal waveform.

Figure 5. PZT signal from the impact of a 1.8×10^{-14} kg particle at 2.76 kms^{-1} (momentum 4.9×10^{-11} Ns).

The measured signals (in V) were normalised by the momentum of the incident particle (in Ns) and plotted (Figure 6). A least-squares fit was then performed for the function

7

$$S = a \qquad v < v_o$$
$$S = a + b(v-v_o) \qquad v > v_o$$

where a, b and v_o are constants. A linear fit has been assumed since the scatter on the data and the limited velocity range do not warrant a more complicated function. a represents the PZT sensitivity (mV/Ns) and v_o the threshold velocity for ejecta formation (and hence momentum enhancement).
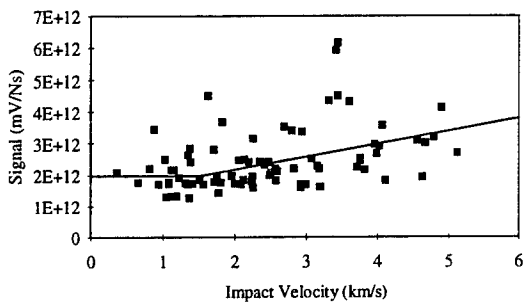

Figure 6. PZT signals normalised with respect to the projectile momentum, plotted against impact velocity. The solid line is the least squares fit.

The PZT sensitivity was derived as 1.97 x 10^9 V/Ns. The average rms noise level recorded was 2.9 mV, so a signal-to-noise criterion of 3:1 corresponds to a signal of 8.7 mV and a momentum of 4.4 x 10^{-12} Ns. For the mass-velocity dependence of the dust accelerator this corresponds to a velocity of ~5 kms^{-1}. The fact that some events are recorded above this velocity is due to the statistical variation in particle masses (and hence momenta) at given velocities and to the onset of momentum enhancement.

The threshold velocity v_o was derived as 1.5 ± 0.2 kms^{-1}. Slattery and Roy[16] and Stradling et al.[17] assume the onset of momentum enhancement to occur when the impact velocity exceeds the speed of sound in the material. Our value of 1.5 kms^{-1} is clearly inconsistent with this and is more in keeping with the findings of Rembor[7] who used 1 mm thick aluminium plates as targets

and derived values of 1.5 to 2.5 kms^{-1} depending on angle of incidence.

Dividing the normalised signals (in Figure 6) by the PZT sensitivity gives the momentum enhancement. This was derived for each event and the average calculated for velocity bins. The results are shown in Figure 7 along with the calculated fit. The observed gradient is 0.21 skm^{-1}. This is in very close agreement with Slattery and Roy[16] and Stradling et al.[17] who both derived values of ~2 skm^{-1}, while Rembor[7] derived values ranging from 0.2 to 0.78 skm^{-1}.
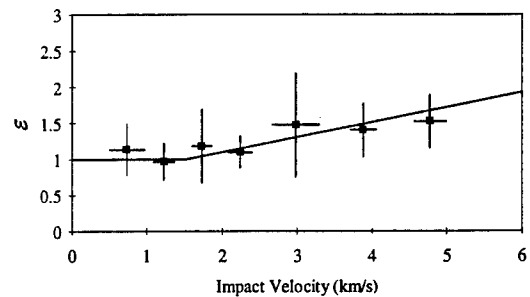

Figure 7. Momentum enhancement. Error bars are the standard deviation of the binned data.

Impact Plasma

The plasma yield from primary impacts of iron particles on rhodium, normalised to the mass of the impacting particle, is shown in Figure 8. The equation fitted to the data is

$$Q/m = 8.54 \times 10^{-3} \, v^{4.74}$$

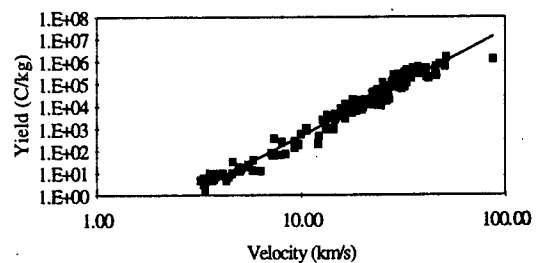with Q in Coulombs, m in kilograms and v in kms^{-1}.

Figure 8. Primary impact plasma yield.

8

We will assume that this equation also applies to the yield from secondary impacts of the (primarily) rhodium ejecta on the (molybdenum) grid. Implications of this assumption are discussed below.

The yield of secondary plasma, again normalised with respect to mass of the primary projectile, is shown in Figure 9. Here the fit has been derived as
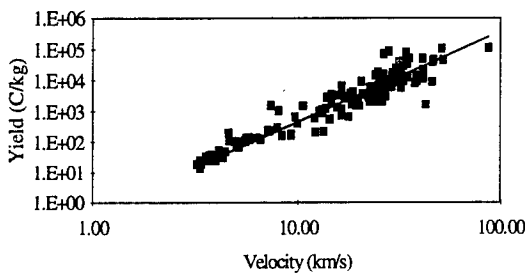
$$Q/m = 0.570v^{2.916}$$

Figure 9. Secondary impact plasma yield.

Allowing for the 85% transparency of the grid resulting in only 15% of the ejecta being seen (the transparency of the grid is in fact weakly dependent on the ejecta trajectory, but the nominal figure will be used),

$$Q/m = 3.8v^{2.916}$$

We use this formula to calculate the secondary ion yield that would have been expected for each of the momentum enhancement events, and then use the primary yield formula as the second simultaneous equation to derive the total ejecta mass and characteristic velocity, and hence kinetic energy.

Ejecta Mass

Calculating in the first instance the mass of ejecta per unit projectile mass we obtain the results shown in Figure 10. The top line is based on the assumption of a constant 45°

average ejection angle, the middle line on Eichorn's data[4] but assuming 30° applies also to high velocities, and the lowest curve uses an extrapolation of Eichorn's observed ejection angle trend with velocity.
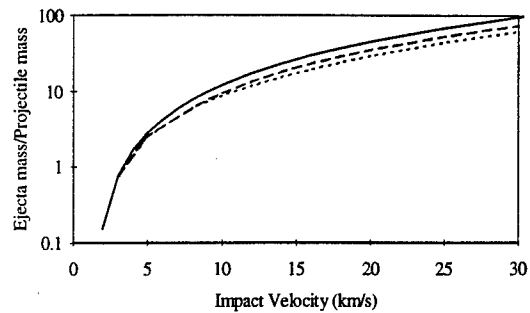

Figure 10. Calculated ejecta masses normalised with respect to projectile mass as a function of impact velocity. Solid line = 45° ejection angle invariant with velocity, dashed line = angle falls from 45° to 30° at 8 kms[-1] but constant thereafter, dotted line = angle falls from 45° to zero.

We see zero ejecta mass below 1.5 kms[-1] impact velocity, rising to equal projectile mass at ~3 kms[-1], and thereafter ejecta must be dominated by target material as the ejecta mass greatly exceeds the projectile mass. The effect of the assumed variation in ejecta angular distribution is small.

Converting these ejecta masses into crater volumes and assuming hemispheric form, we can compare the results with those predicted by published cratering equations. Figure 11 shows a comparison of calculated crater diameter normalised with respect to projectile diameter as a function of impact velocity. Plotted for comparison are predictions based on the crater diameter equation of Watts et al.[3] and on the foil penetration formula of McDonnell and Sullivan[18] (assuming a ratio of 1.5 between foil thickness at the ballistic limit and equivalent semi-infinite target crater depth).

The two theoretical lines demonstrate the wide range that current predictive capability

9

still allows. In view of this our derived values are reasonable. We would expect our estimates to be lower than the true values as we do not allow for crater excavation by any means other than material ejection. No account is taken of material compaction or plastic deformation and so we derive a zero crater volume for low velocity impact.
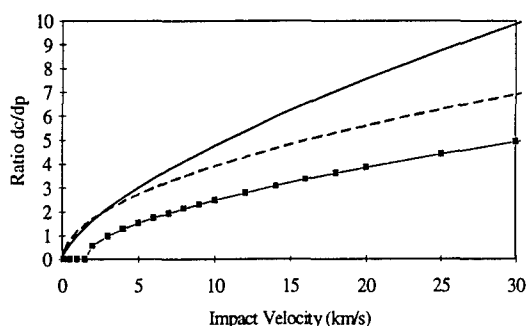

Figure 11. Calculated crater diameter, normalised with respect to the projectile diameter, based on experimental data (for constant 45° ejection angle) and two theoretical equations. Solid line = McDonnell and Sullivan[18], dashed line=Watts et al.[3].

Ejecta Velocities

The ejecta masses derived above imply characteristic ejection velocities as shown in Figure 12.
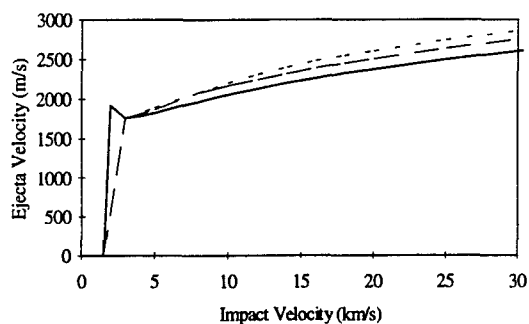

Figure 12. Characteristic ejecta velocities vs impact velocity. Solid line = 45° ejection angle invariant with velocity, dashed line = angle falls from 45° to 30° at 8 kms^{-1} but constant thereafter, dotted line = angle falls from 45° to zero. The apparent difference below 3 kms^{-1} is due to the absence of a 2 kms^{-1} datum in the latter two data sets.

The zero ejecta velocity for impact velocities below 1.5 kms^{-1} simply reflects the absence of ejecta. We then obtain a characteristic ejecta velocity of around 2 kms^{-1} with only a relatively weak dependence on the impact velocity. This is to be expected. While the maximum ejecta velocity would be expected to rise with increasing impact velocity, the minimum ejecta velocity occurs when the shock wave strength only slightly exceeds the strength of the material. For any impact velocity we thus expect to see low velocity ejecta, and its presence moderates the dependence of the characteristic velocity on the impact velocity. Again the dependence on the assumed angular distribution of ejecta is weak.

Energy Partitioning

The implication of the derived ejecta masses and velocities for the ejecta kinetic energies are shown in Figure 13. The ejecta kinetic energy is expressed as a percentage of the incident particle kinetic energy as a function of impact velocity.
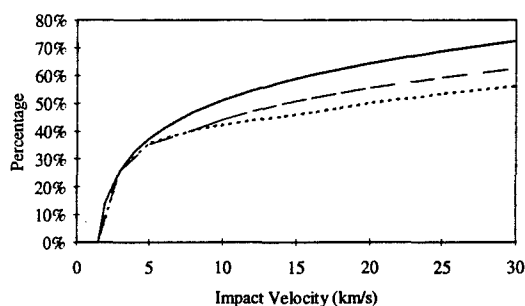
Figure 13. Partitioning of the projectile kinetic energy to ejecta kinetic energy as a function of impact velocity. Solid line = 45° ejection angle invariant with velocity, dashed line = angle falls from 45° to 30° at 8 kms^{-1} but constant thereafter, dotted line = angle falls from 45° to zero.

Again we see that the influence of the assumed ejecta angular distribution is weak. The percentage of the projectile kinetic energy converted to ejecta kinetic energy

10

rises rapidly when the threshold velocity of 1.5 kms^{-1} is exceeded and flattens off at higher velocity. This form is palpably correct - the value must be zero at low velocities where no ejecta is produced and can not exceed 100% at any velocity. However, the absolute values require some further consideration.

Firstly, when applied to secondary plasma production the 'm' in equation 7 is not strictly the total ejecta mass, but only the integrated mass with velocity greater than the critical threshold velocity for plasma production (~1.5 kms^{-1}). It is well known that for brittle target materials the majority of the ejecta mass is seen to be low velocity spallation[e.g.19], but as a ductile material this will not be the case for rhodium. Eichorn[4] measured ejecta velocities for iron particle impacts on gold, a more comparable system, for impact velocities of 3 to 8 kms^{-1} and found none below ~1.5 kms^{-1}. However, his detection technique was the light emitted on impact and so suffers from a similar velocity threshold selection effect. If the mass in equation 7 is significantly lower than the total ejecta mass, equation 10 tells us that we will have overestimated the ejecta kinetic energy.

Secondly we have to address the question of whether the constants in equation 7 derived for the primary impact apply to the secondary plasma yield. In particular the primary equation was derived for particles with a minimum size of 28 nm whereas secondary plasma is produced by particles with a range of sizes down to single atoms and ions. The inaccuracy introduced by the different materials involved in the primary and secondary impacts will be small as ion yields do not vary greatly for any metal-on-metal impact. The fact that the ejecta will be 'hot' will have an influence which can not be quantified at this stage. Ion yield experiments with heated targets are planned to address this question. If this effect is significant it will result in an underestimate of the ejecta kinetic energy, opposing the mass velocity threshold factor described above.

There is little or no published data directly comparable with our results. Gault and Heitowit[2] measured energy partitioning for aluminium impact in basalt at 6.25 kms^{-1}, and obtained values of 43-53% for ejecta kinetic energy. Our value at 6.25 kms^{-1} is 36-41% depending on the assumed ejecta trajectory distribution. Since metals are ductile one would expect reduced ejecta production (particularly through spallation) and increased plastic deformation compared with brittle materials such as basalt, and so are results appear highly credible.

Discussion

The results described in this paper demonstrate the viability of ejecta kinetic energy measurement based on measurements of momentum enhancement in the primary impact and plasma production by secondary impacts. The data presented represent a pilot test in preparation for using materials of greater relevance to spacecraft applications. One feature of the experiments that will be improved in the later stages of the programme is the threshold (and hence the velocity range) of the momentum measurements.

The technique is open to further refinement. Ejecta trajectory distributions, once defined by independent measurement, can be used instead of the assumed average ejection angles. This will have only a small effect on the results, but by removing one of the unknown parameters will allow the ejecta

velocity distribution to be derived from the time-profile of the secondary plasma signal. This distribution will then be used instead of the assumed 'characteristic' velocity.

The major remaining 'unknown' is the effect of the elevated temperature of the ejecta on the secondary plasma yield. Experiments are planned, using heated targets, to quantify the uncertainty that this effect will have on the results. However, in order to include the effect in the analysis involves including a fourth variable (temperature) in the characterisation of ejecta (in addition to mass, velocity and trajectory). Measurement of ejecta temperature (through time and spatially resolved light emission) is feasible, but represents a long-term objective of the study.

Acknowledgements

References

[1] R.D. Caswell, N. McBride and A.D. Taylor, 'Olympus End of Life Anomaly - A Perseid Meteoroid Impact Event?', presented at the Hypervelocity Impact Symposium, Santa Fe, NM, October 17-19 (1994).

[2] D.E. Gault and E.D. Heitowit, Proc. Symp. Hypervel. Impact 6th 2, pp. 419-456, (1963).

[3] A.J. Watts and D. Atkinson, 'Dimensional Scaling for Impact Cratering and Perforation', presented at the Hypervelocity Impact Symposium, Santa Fe, New Mexico, 17-19 October, 1994.

[4] G. Eichorn, 'Primary Velocity Dependence of Impact Ejecta Parameters', Planet. Space Sci. 26, pp. 469-471 (1978).

[5] S.K. Croft, 'Hypervelocity Impact Craters in Icy Media', Lunar Planet. Sci. XII, pp. 190-192, (1981).

[6] J.M. Thomsen, M.G. Austin and P.H. Schultz, Lunar Planet. Sci. XI, pp. 1146-1148, (1980).

[7] K.M. Rembor, 'Momentum Exchange at Particle Impacts - A Calibration Study for the Giotto/DIDSY Momentum Sensors', Diploma Thesis, University of Kent at Canterbury, 1993.

[8] G. Eichorn and E. Grün, 'High Velocity Impacts of Dust Particles in Low-Temperature Water Ice', Planet. Space Sci. 41, pp. 429-433 (1993).

[9] M.J. Burchell, M.J. Cole, J.A.M. McDonnell and P.R. Ratcliff, "The Hypervelocity Impact Facilities at the University of Kent, UK", Lunar and Planetary Institute Technical Report 94-05, pp. 32-35 (1994).

[10] P.R. Ratcliff, J.A.M. McDonnell, J.G. Firth and E. Grün, 'The Cosmic Dust Analyser', J. Brit. Interplanetary Soc. 45 No. 9, pp. 375-380 (1992).

[11] E.L. Christiansen, E. Cykowski and J. Ortega, 'Highly Oblique Impacts into Thick and Thin Targets', Int. J. Impact Engng 14, pp. 157-168 (1993).

[12] N.G. Mackay, S.F. Green, D.J. Gardner and J.A.M. McDonnell, 'Experimental Investigation of the Relationship Between Impact Crater Morphology and Impacting Particle Velocity and Direction', 3rd LDEF Post-Retrieval Symp., Williamsburg, 1993.

[13] J.A.M. McDonnell, D.J. Gardner, P.J. Newman, N.J. Robertson and C.J. Hayhurst, 'Hydrocode Modelling in the Study of Space Debris Impact Crater Morphology', Proc. 1st European Conf. on Space Debris, Darmstadt, Germany, pp. 425-432 (1993).

[14] C.J. Hayhurst, H.J. Ranson, D.J. Gardner and N.K. Birnbaum, 'Modelling of Microparticle Hypervelocity Oblique Impacts on Thick Targets', presented at the Hypervelocity Impact Symposium, Santa Fe, New Mexico, 17-19 October, 1994.

[15] P.R. Ratcliff, F. Gogu, E. Grün and R. Srama, "Plasma Production by Secondary Impacts: Implications for Velocity Measurements by In-Situ Dust Detectors", Adv. Space Res. 14 (in press).

[16] J.C. Slattery and N.L. Roy, 'Investigations of Hypervelocity Impact Phenomena', NASA CR-66872 or Report 11489-6012-RO-OO, TRW Systems Group, Redondo Beach, CA, (1970).

[17] G.L. Stradling, G.D. Idzorek, P.W. Keaton, J.K. Studebaker, A.A. Hopkins Blossom, M.T. Collopy, H.L. Curling Jr. and S.D. Bergeson, 'Searching for Momentum Enhancement in Hypervelocity Impacts', Int. J. Impact Engng 10, pp. 555-570, (1990).

[18] J.A.M. McDonnell and K. Sullivan, 'Hypervelocity Impacts on Space Detectors: Decoding the Projectile Parameters', in: Hypervelocity Impacts in Space, ed. J.A.M. McDonnell, University of Kent at Canterbury, pp. 39-47, (1992).

[19]W. Frisch, 'Hypervelocity Impact Experiments with Water Ice Targets', in: Hypervelocity Impacts in Space. ed. J.A.M. McDonnell, University of Kent at Canterbury, pp. 7-14, (1992).

EXPERIMENTAL MEASUREMENTS OF HYPERVELOCITY IMPACT PLASMA YIELD AND ENERGETICS

PAUL R. RATCLIFF[†], MARK J. BURCHELL[†], MIKE J. COLE[†], TOM W. MURPHY[†], and FIROOZ ALLAHDADI[‡]

[†]Unit for Space Sciences and Astrophysics, Physics Laboratory, University of Kent at Canterbury, Canterbury, Kent CT2 7NR, U.K.; [‡]US Air Force, Space Kinetic Impact and Debris Branch, PL/WSCD, Phillips Laboratories, Kirtland AFB, Albuquerque, NM 87117, USA.

Summary—Ion yields and their characteristic energies have been measured experimentally in the plasma produced by hypervelocity impacts of iron microparticles on rhodium in the range 1.2 to 87 km s^{-1}. The ion yield shows a greater velocity dependence than has generally been reported in the literature, though the difference is attributed to experimental and analytical effects. The higher value derived here is believed to be a better representation for the yield of plasma from the primary impact. The impact plasma is shown not to be in thermal equilibrium. Characteristic energies of the target and projectile material ions typically lie in the range 20-40 eV (also higher than values generally quoted in the literature) and show little variation with impact velocity, while contaminant ions (alkali metals and hydrogen) show significantly different trends indicating a different production mechanism.

NOTATION

A	constant of proportionality between t_a and $\sqrt{m}$
B	constant of proportionality between t_d and $\sqrt{m}$
C	constant of proportionality between t_i and $\sqrt{m}$
c	constant
D	constant of proportionality between t_f and $\sqrt{m}$
E	energy
l_a	length of the acceleration region of the spectrometer (3.3 mm)
l_d	length of the drift region of the spectrometer (190 mm)
m	mass
Q	ion yield
q	ion charge
t_a	ion time-of-flight through the acceleration region of the spectrometer
t_d	ion time-of-flight through the drift region of the spectrometer
t_f	total ion time-of-flight
t_i	ion time-of-flight from the screen grid to the electron multiplier
V_a	target potential
v	velocity
α	constant
β	constant
ΔE	ion energy
Δt_f	offset of spectral line from its nominal position

INTRODUCTION

The phenomenon of plasma production by hypervelocity impact was first reported by Friichtenicht and Slattery over 30 years ago [1]. Since then extensive experimental investigations have established reliable empirical relationships describing plasma yield (as a function of impactor mass and velocity and of impactor and target materials, e.g. [2], [3], [4], [5]), and theoretical descriptions of the process (or rather processes, as the emission mechanism of ions from the surface of the impactor and target can be different to that for ions from the bulk material) have been developed based on either continuum mechanics (e.g. [6]) or thermodynamics (e.g. [7]). While both these theories go a long way towards describing impact plasma production, as yet neither provide predictions in complete agreement with experimental measurements. A fundamental difference between the implications of these theories is the energetics of the ions produced and whether or not an equilibrium or far-from-equilibrium state exists at short times after ion production. However, experimental investigations of impact plasma energetics have so far been extremely limited: Friichtenicht et al. [8] derived plasma temperatures from the degree of ionisation seen for the different species in a multi-element target via the Saha equation (thus assuming thermal equilibrium in the plasma) and quote values of ~0.5 eV invariant with velocity over the range 17-47 km s^{-1}. Krüger and Kissel [3] quote energies "in the few eV regime, at least less than 10 eV", but do not explain the method of derivation, while Krüger [4] assesses expected energy and angular distributions by comparison with other excitation mechanisms (laser irradiation, fission fragment induced desorption and secondary ion mass spectrometry). Ratcliff and Allahdadi [9] derived larger energies (10s eV) for individual ion species observed in a spectrum from a single 94 km s^{-1} impact event, based on the line profiles in a time-of-flight spectrum.

In this paper the results of experiments performed recently at the Hypervelocity Impact Facility at the University of Kent at Canterbury are described.

METHOD

The Dust Accelerator Facility

The University of Kent dust accelerator has been fully described elsewhere [10, 11] so only a brief summary will be included here. A reservoir of micron and sub-micron dust particles is mounted in the positive terminal of a Van de Graaff generator which runs at up to 2 MV. The dust particles are charged (typically to ~ 10^{-14} C) by contact with a needle which is at a potential of 15 kV with respect to the terminal, and are accelerated through the 2 MV potential well defined along the beam line by field-grading rings. The kinetic energy of the particles is the product of their charge and the accelerating potential, and so there is a strong correlation between particle velocity and mass (see Fig. 1). The facility thus provides a stream of particles to the experiment chamber at an average rate of up to one per second, while the distribution of masses (and hence velocities) is defined by the size distribution of the particles in the dust sample. The option of velocity selection is available (by deflecting the beam off axis electrostatically unless a particle is detected with the required velocity), but for the current investigation all particles were accepted and real-time measurements of the mass and velocity of the particle made for each plasma-producing event.

Experiment Configuration

The experiment configuration (Fig. 2) is that of a simple linear time-of-flight mass spectrometer. The target assembly was mounted in a vacuum chamber which has an internal diameter of 30 cm and has 10 ports at 36^{a} intervals around the side. The dust particle beam was

admitted to the chamber through one of these ports and the particles impacted on the target. The target consisted of a 25 μm thick rhodium foil (i.e. a semi-infinite target to the micron and sub-micron particles) bonded (with conductive epoxy resin) to a 0.5 mm thick aluminium plate, which was in turn mounted on a perspex block. The target was maintained at a positive potential. A fine grid (~270 μm pitch, 85% transparency) was mounted 3.3 mm in front of the target. This was electrically isolated from the target and was earthed. A planar electric field was thus sustained above the surface of the target which resulted in the electrons (and/or negative ions) being collected on the target (from which the signal is recorded) and the positive ions being accelerated in the direction of the target normal. The target was inclined at an angle of $36°$ to the incident particle beam so that the positive ions were focused on an electron multiplier mounted in a tube attached to another port in the chamber. This angle is not expected to cause the results to differ from the case of normal incidence since Krüger [4] found no difference in ion yield or energy and angular distributions for impacts at an angle of $45°$. Also, this angle is not great enough to cause elliptical craters to be produced [e.g. 12, 13, 14, 15] and so one would not expect a significant difference in plasma production compared with normal incidence impacts.
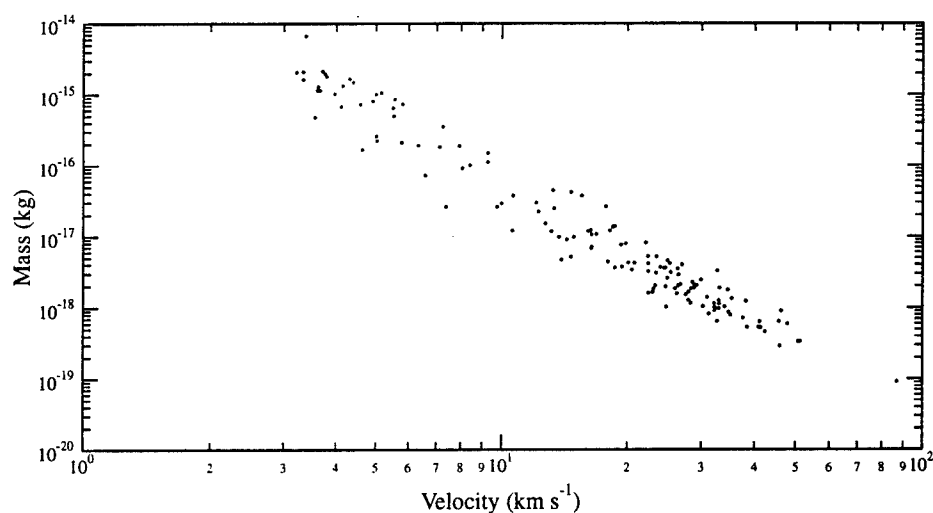

Fig. 1. Accelerator mass-vs-velocity plot for the data included in the current study.
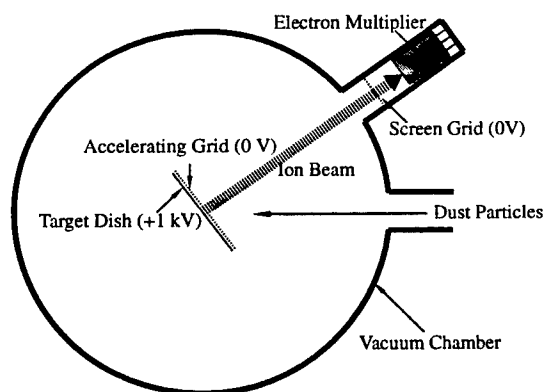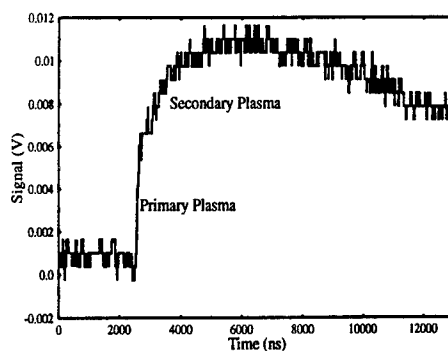

Fig. 2. Experiment configuration.

Fig. 3. Sample target signal showing the primary ion yield and that due to secondary impacts on the accelerating grid.

The kinetic energy imparted to the positive ions by the accelerating field is the product of their charge and the accelerating voltage and so their velocity is a function of their charge-to-mass ratio. For impacts in the velocity range investigated only singly-charged ions are produced and so their velocity, and hence time-of-flight to the electron multiplier, is simply a function of their

mass. In a conventional spectrometer, energy focusing is used to cancel (at least to first order) the contribution of the initial (thermal/kinetic) energy of the ions to their time of flight in order to maximise the mass resolution of the system. However, by adopting a simple geometry the ions' initial energy contributes to their time-of-flight and so the offset of the observed line positions from their theoretical location provides a direct measurement of their energy.

RESULTS AND ANALYSIS

Total Ion Yield

The total ion yield is derived from the target signal, an example of which is shown in Fig. 3. The signal has two distinct components: a fast-rising (10s ns) leading edge due to plasma produced in the primary impact and a slow (several μs) component due to plasma produced by ejecta hitting the accelerating grid. The time constant of the fast component is determined by the strength of the accelerating field, but the time constant of the slow component is determined by the times-of-flight of ejecta particles between the target and the grid and is thus a function of the impact velocity. If the accelerating field is large, such that ion times-of-flight between the target and grid are short compared with ejecta particle times-of-flight, the two components are clearly resolvable. Accelerating potentials of 500 V and 1 kV have been used in the current investigation.

The yield of plasma, expressed as a function of impactor mass and velocity, is described by the standard empirical equation:

$$Q = cm^{\alpha}v^{\beta}$$

where Q is the ion yield, m is the impactor mass, v the impact velocity, and c, α and β are constants.

Although a value of α of 0.8 has been preferred by some authors (e.g. [3, 4]) based on experimental results, and Kissel and Krueger [5] predict values less than unity based on theoretical considerations, Göller and Grün [16] (whose data set of 10^5 impacts represents by far the most extensive investigation so far) found that the best statistical fits to their data were obtained for $\alpha = 1$. We also find a better fit for $\alpha = 1$ (regression coefficient $R^2 = 97.57\%$ compared with 96.27% for $\alpha = 0.8$) and thus adopt the value of unity. Figure 4a shows the integrated ion yield, normalised by particle mass, as a function of impact velocity.

The values derived for the constants c and β are 8.5×10^{-3} and 4.74 respectively (for Q measured in Coulombs, m in kg and v in km s^{-1}). This value of β is large compared with published values for impacts on other metals [e.g. 2, 3, 4, 5] which typically lie in the range 3.5 - 4. However, it is believed that this reflects discrepancies in experimental configuration and analysis rather than a true difference in the ion yield velocity-dependence for rhodium. Kissel and Krueger [5] and Krueger [4] adopt $\alpha = 0.8$ (based on their theoretical arguments that α should be less than unity and following an earlier empirical result they attribute to Dietzel et al. [2] who, however, used $\alpha = 1$). A lower value for α results in a lower derived value for β — we obtain $\beta = 4.1$ for $\alpha = 0.8$. Dietzel et al. [2] and Göller and Grün [16] (who do not quote a value for β, but a value of ~3.5 is evident from their Fig. 6) use $\alpha = 1$, but in their experiment configuration the plasma from secondary impacts is not distinguishable from that from primary impacts [17]. If the secondary impact plasma is included in our analysis (Fig. 4c) the value of β falls to 3.88 because the velocity exponent of the secondary ion yield on its own is only 2.74 (Fig. 4b) because the characteristic velocity of ejecta has only a small dependence on the impact velocity [e.g. 18, 19]. The primary and secondary yield are equal at a velocity of 10.6 km s^{-1}, which results in a change in the gradient of the total ion yield graph (Fig. 4c) at this point.
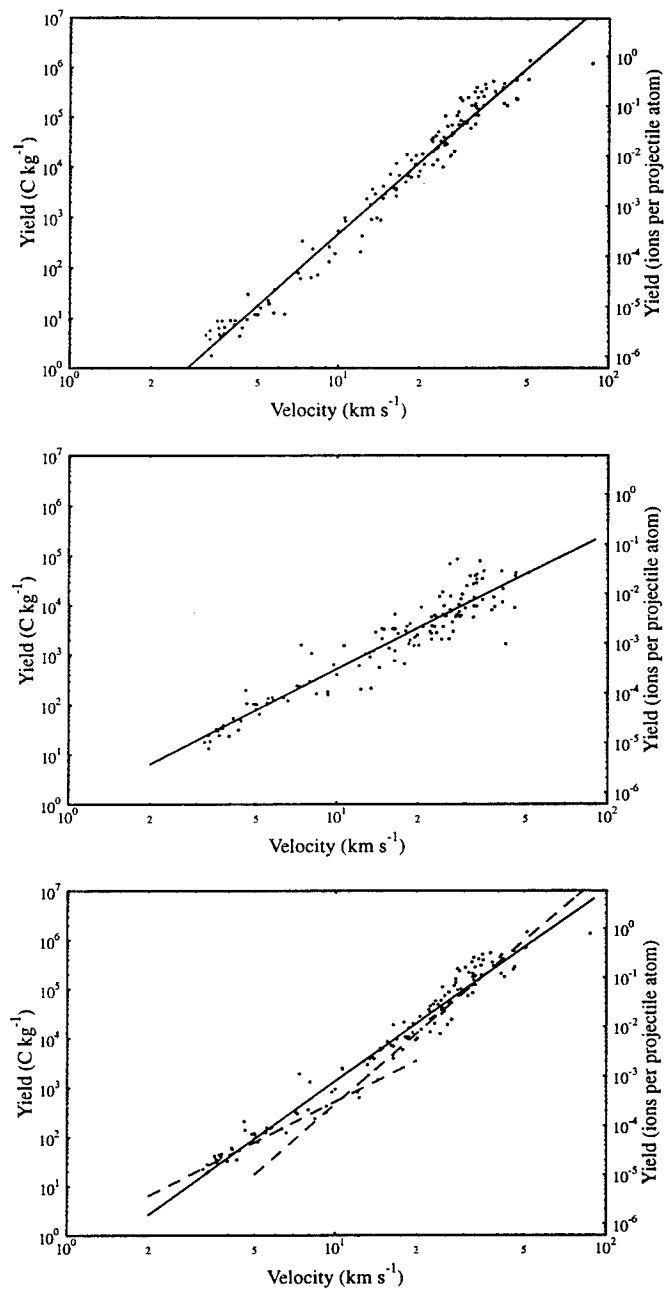
Fig. 4. Ion yields. a) Yield from the primary impact (target signal fast component) with least squares fit. b) Yield from secondary impacts (target signal slow component) with least squares fit. c) Total yield (primary plus secondary) with least squares fit (solid line) and fits to primary and secondary yield (dashed lines).

Species Ion Yields

The relative yields of the different atomic species observed in the impact plasma have also been derived (Fig. 5). The threshold for detection of lines in mass spectra is determined by the transmission of the accelerating and screen grids, by the aperture of the electron multiplier compared with the ion beam spot size and by the signal-to-noise ratio of the amplified signal. The threshold corresponds to $\sim 10^4$ ions generated at the target, so the threshold in terms of ions per

projectile atom (or mass) is a function of impact velocity due to the mass-velocity relationship of the accelerator.
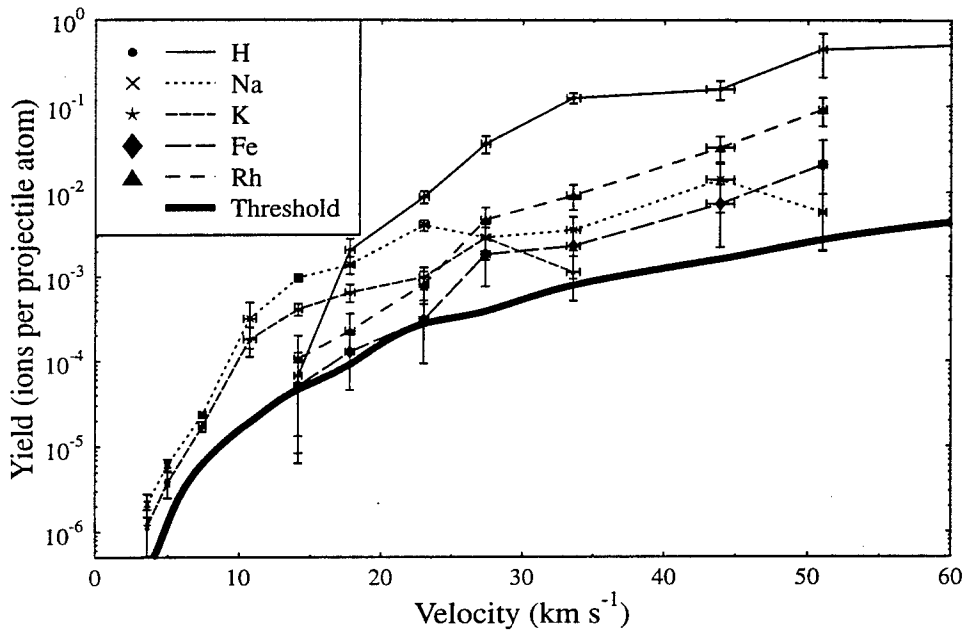

Fig. 5a. Yields of the 5 most abundant ion species - number per dust particle atom.
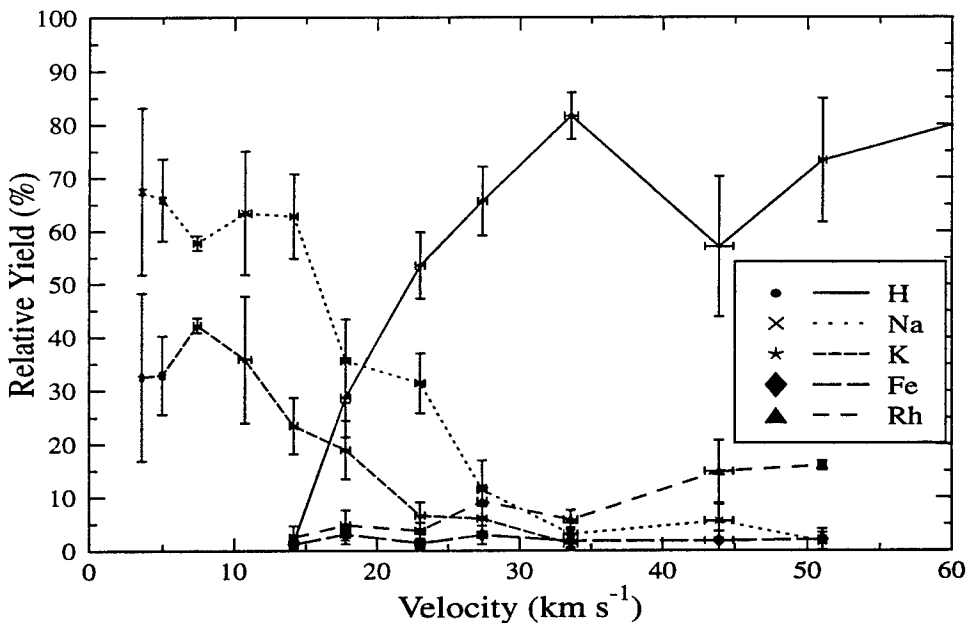

Fig. 5b. Yields of the 5 most abundant ion species - percentage of total yield.

The plasma is dominated at low velocities (below 15 km s^{-1}) by the alkali metals sodium and potassium, which are almost impossible to eradicate as contaminants in the system and are highly visible in spectra due to their low ionisation energy. This result has been reported previously, e.g. by Dalmann et al. [20]. Above 20 km s^{-1} hydrogen is the dominant species (as reported by Krüger and Kissel [21]), and iron and rhodium from the projectile and target also become significant. The yield of sodium and potassium drops rapidly as a proportion of the total above 15 km s^{-1}.

The yield of sodium has little velocity dependence above 20 km s^{-1}, and potassium is rarely seen in impacts above 30 km s^{-1}. This implies that the alkali metals may be produced by a different process than the target and projectile material, and may reflect the change from surface processes to bulk ionisation of the projectile and target.

Species Energies

In order to calculate the initial energy of the ions it is necessary to calculate the nominal (i.e. zero energy) positions of lines in a mass spectrum. The ion trajectory can be divided into three parts: the "acceleration region" between the target and the accelerating grid, the "drift region" between the accelerating grid and the multiplier screen grid, and the "multiplier infall region" between the screen grid and the front dynode of the electron multiplier.

The electric field in the acceleration region is planar and in the drift region is zero, so the ion times-of-flight in these regions are trivial to calculate:

$$t_a = \frac{2l_a}{\sqrt{2V_a q / m}} \tag{1}$$

and

$$t_d = \frac{l_d}{\sqrt{2V_a q / m}} \tag{2}$$

where t_a is the time taken to traverse the acceleration region, l_a is the separation of the target and acceleration grid (3.3 ± 0.2 mm), V_a is the potential of the target relative to the acceleration grid, q is the charge of the ion (+1 electron charge), m is the ion mass, t_d is the time taken to traverse the drift region and l_d is the length of the drift region (190 ± 5 mm). Hence,

$$t_a = A\sqrt{m} \qquad \text{where } A = \frac{2l_a}{\sqrt{2V_a q}} \tag{3}$$

$$t_d = B\sqrt{m} \qquad \text{where } B = \frac{l_d}{\sqrt{2V_a q}} \tag{4}$$

The time taken to traverse the multiplier infall region, t_i, will be given by:

$$t_i = C\sqrt{m} \tag{5}$$

where C is a constant determined by the field in this region. This field is not directly calculable but has been modelled using the SIMION ion optics software package (Fig. 6). A 3rd order polynomial can be derived which describes the on-axis field strength, but it is simpler to derive the value of C by using SIMION to measure t_i for a hydrogen ion.

The total time-of-flight of ions from the target to the electron multiplier is then:

$$t_f = D\sqrt{m} \tag{6}$$

where $D = A + B + C$, the values of which are only a function of the accelerating voltage (the multiplier voltage was kept at -3 kV). The values of these constants are shown in Table 1 for the accelerating voltages used.

Table 1. Values of the constants A, B and C for accelerating voltages of 500 and 1000 V for ion mass, m, measured in atomic mass units and t in μs.

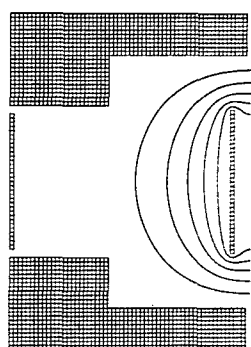|	$V_a = 500$ V	$V_a = 1$ kV
A	0.021	0.015
B	0.617	0.433
C	0.125	0.098
A+B+C = D	0.763	0.546

Fig. 6. Electric field in the multiplier infall region. The line at the left-hand-side is the multiplier screen and that near the right-hand-side is the front dynode of the multiplier. Shaded areas are the walls of the vacuum chamber. Contours of equal electrostatic potential are shown at intervals of 500 V.

If the approximation is made that the ion velocity is constant throughout its flight, then its kinetic energy is :

$$E = \frac{1}{2}mv^2 \tag{7}$$

and substituting for m from Eqn. (6) gives:

$$E = \frac{v^2 t_f^2}{2D^2} \tag{8}$$

and hence by standard error propagation theory:

$$\frac{\Delta E}{E} = 2\frac{\Delta t_f}{t_f} \tag{9}$$

where ΔE is the component of the initial thermal/kinetic energy of the ion in the direction of the target normal, E is the energy imparted by the electric field and Δt_f is the shift of the line from its nominal position in the mass spectrum.

The error in ΔE introduced by making this approximation is small. The relative values of the constants A, B and C (Table 1) show the relative times ions spend in each of the three regions of the spectrometer. The majority of the time-of-flight (79% for 1 kV accelerating field and 81% for 500 V) is spent in the drift region where the ion velocity is constant. Also, due to the configuration of the field in the multiplier infall region, this velocity only changes significantly once the ion is close to the electron multiplier. Figure 7 shows the velocity of a hydrogen ion as a function of position in the spectrometer and of time during its flight. The approximation that the velocity of the ion is constant throughout the spectrometer and is equal to the drift velocity results in a calculated time-of-flight only ~3% (in the case of 1 kV accelerating field) longer than the actual value.
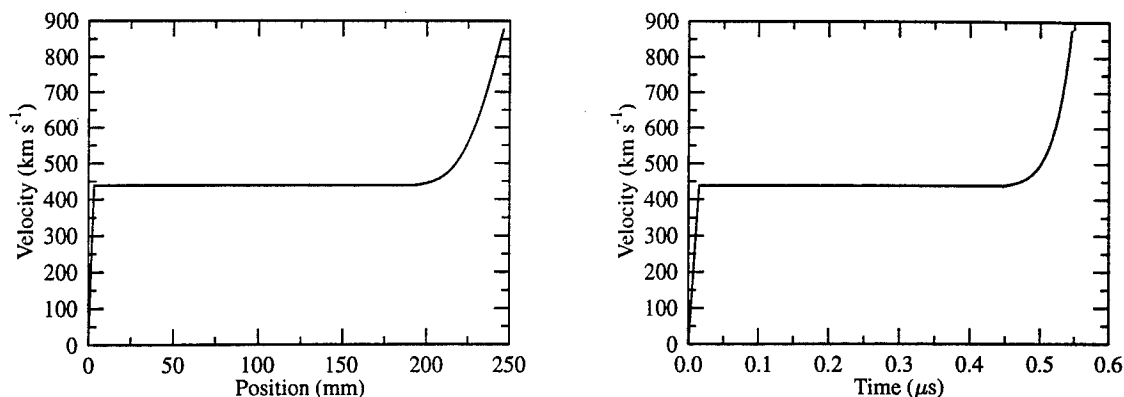
Fig. 7. Hydrogen ion velocity as a function of position in the spectrometer (a) and time during flight (b).

Figure 8 shows a sample spectrum from the electron multiplier. The times of the peaks of the spectral lines relative to the target signal can be measured readily. This time is the sum of the ion times of flight, the signal propagation time through the electron multiplier and any time delays introduced in the processing electronics - these latter two components have been measured as 30 ± 5 ns. This value is comparable to the shift of the lines in the mass spectrum from their nominal position, and so the values derived for the ion energies depend on the exact value adopted for the electronics delay. In order to verify the measured value, the experiment was performed using two values of the accelerating voltage, 1 kV and 500 V, and hence two values of E in Eqn. (9). Any error in the measurement of the electronics delay time would be exposed by inconsistent values of ΔE derived from the two data sets.
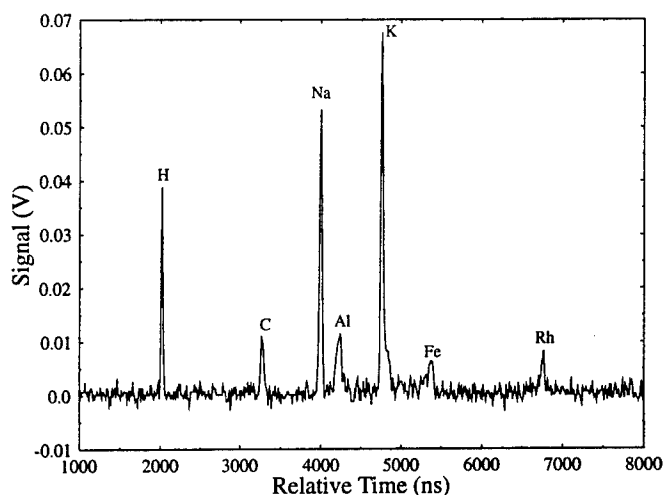

Fig. 8. Sample mass spectrum showing 7 ion species. Iron and rhodium are from the projectile and target respectively. Hydrogen, carbon, sodium and potassium are present as contaminants in the system. The line at mass 27 could be due to either aluminium or (less probably) the organic cluster ion $C_2H_3^+$, or a combination of both.

The optimum value of the accelerating field involves a trade-off between conflicting considerations. The precision of the measurement of $\Delta t_f/t_f$ is clearly enhanced if the time-of-flight is large (i.e. the accelerating field is small) while the variation in the ratio $\Delta E/E$ with ΔE is greatest for $\Delta E \approx E$. This would imply that the accelerating potential should be a few 10s of volts. However, for low voltages the detection threshold of the electron multiplier is lowered by two

factors: the focusing of the ions is reduced so fewer ions reach the multiplier and the spectral lines are broadened so their peak heights are reduced. The accelerating voltages used provide reasonable results, but the optimum value has not yet been derived.

Figure 9 shows the characteristic energies of the different atomic species observed in the impact plasma. The energy of the rhodium ions lies in the range 20-30 eV and shows little dependence on impact velocity. The iron ion energies appear to be generally higher at around 35 eV, but the statistics are relatively poor as yet. The hydrogen ions do have a systematically higher energy of 55 ± 13 eV, again with no noticeable trend with impact velocity. The energies of the alkali metal lines, however, show an inverse dependence on impact velocity. Their energies peak at 40-50 eV for impacts at around 5 km s^{-1}, but fall with increasing impact velocity to 10-20 eV at 30 km s^{-1}. At higher impact velocities the energy of the sodium ions may rise slightly, but may also be invariant with velocity within the precision of the measurements. The yield of potassium for impacts above 35 km s^{-1} is too low to make further measurements.
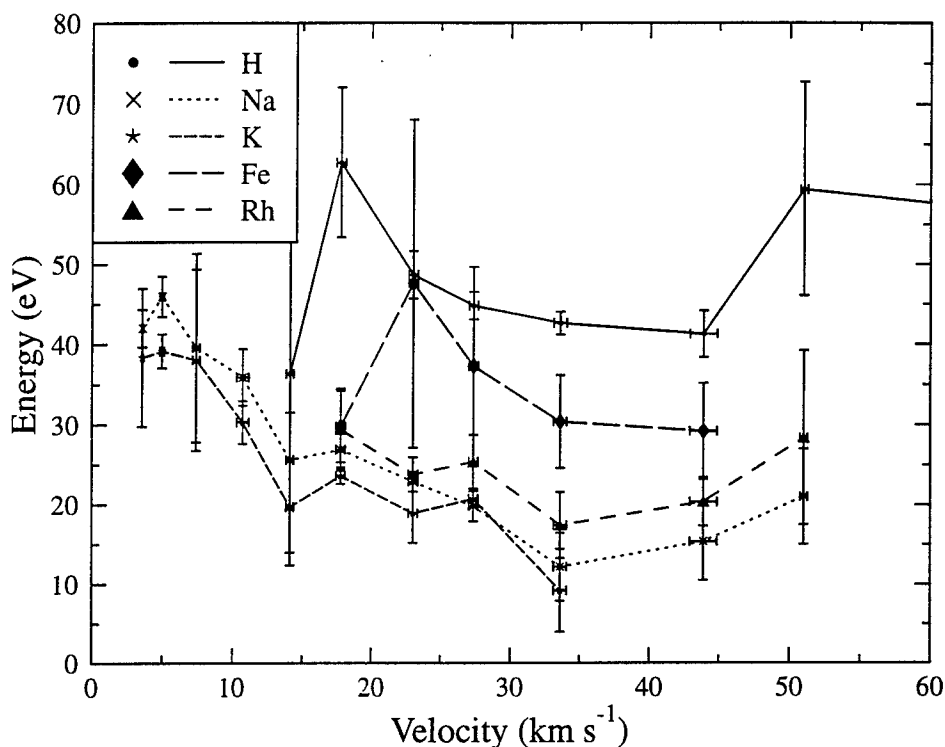

Fig. 9. Ion energies for the 5 most abundant ion species.

The differing results for different species suggest that the plasma is not generated in a state of thermal equilibrium and that equilibrium is not established on the timescale of ion extraction by the applied electric field (sub ns), and hence that the degree of ionisation can not be described by the Saha equation. The inverse relationship between the impact velocity and the energy of the alkali metal ions again implies their production by a different physical process.

CONCLUSIONS AND DISCUSSION

The yield and energetics of the plasma produced by iron microparticle impacts on rhodium have been measured. The velocity-dependence of the total ion yield, expressed as the exponent β, has been found to be greater than has been published by previous authors [2, 3, 4, 5, 16] for iron

particle impacts on other metallic targets. However, this is attributed to differences in experiment geometry and analysis rather than to properties of rhodium. Previous published results [e.g. 2, 16] have been based on studies which do not distinguish between plasma produced by the primary impact and that produced by subsequent impacts of ejecta. If the secondary plasma is included in our analysis, the value of the velocity exponent falls to 3.88, consistent with previously published results. Since the experiment geometry used in this study does allow the primary impact plasma to be distinguished, it is concluded that the value derived here (4.74) is a true measure of the velocity-dependence of the ion yield from the primary impact.

The elemental constituents of the impact plasma have been found to be comparable with published results [20, 21], namely that alkali metals dominate at low velocities while hydrogen and the projectile and target materials dominate at high velocities. Hydrogen, iron and rhodium exceed the detection threshold at velocities of ~15 km s^{-1} and the strong velocity dependence of their yield at this velocity suggests that the velocity threshold for their production is not significantly lower than this. The yield of iron ions is a factor of three lower than the yield of rhodium ions and a factor of 20 lower than that of hydrogen ions, only reaching ~2% of the number of atoms in the dust particle at velocities of ~50 km s^{-1}. However, Krüger [4] suggests that ions from the projectile may be emitted in specular directions relative to the impact angle, which would result in a lower detection efficiency for iron ions than for target ion species in our experiment.

The experiment technique only allows measurement of the component of the ion energy in the direction of the target normal. However, it has been reported elsewhere [3, 4, 9] that the ion trajectories are focused in the direction of the target normal to a degree exceeding a cosine distribution, and since the plasma is not in thermal equilibrium (and hence must be essentially collisionless) the derived values represent a good measure of the kinetic energy of the ions as they are produced. The values derived (10s eV) are larger than have been reported by some authors. Friichtenicht and Slattery [1] derived values of 0.5 eV for iron (Fe), molybdenum boride (MoB) and nickel aluminide (NiAl) particle impacts on a lead/titanium/zirconium target, but this derivation was based on the assumption of thermal equilibrium in the impact plasma. Since their accelerating field (3 kV over 1 cm) was the same as was employed in the current investigation (1 kV over 3.3 mm) this assumption seems invalid. Krüger and Kissel [3] state that energies are in the few eV regime although the high energy tail of the distribution may exceed 10 eV slightly. However, Krüger [4] states that the energy distribution of metallic target ions is several tens of eV broad and that, by comparison with thermal and fission fragment induced desorption, the hydrogen ions may have an energy of 10-20 eV with the high energy tail extending up to 100 eV. The tendency of hydrogen ions to have a higher energy than other species in the same spectrum was also observed by Ratcliff and Allahdadi [9].

In summary, the results obtained for iron impacts on rhodium show that the plasma is not produced in a state of thermal equilibrium and does not reach equilibrium on the timescale of ion extraction by the applied electric field. Elemental analysis of the plasma is in qualitative agreement with published data for other metallic targets, but the velocity dependence of the ion yield and the energies of the ions are generally higher than have been reported elsewhere. Explanations for this have been proposed, and investigations using other target materials have been, and are being, performed to test these theories. These results will be published in a future paper.

REFERENCES

1. J.F. Friichtenicht and J.C. Slattery, Ionization associated with hypervelocity impact, NASA TN D-2091 (1963).
2. H. Dietzel, G. Eichhorn, H. Fechtig, E. Grün, H.-J. Hoffmann and J. Kissel, The HEOS 2 and HELIOS micrometeoroid experiments, *J. Phys. (E) Scientific Instrum.* 6, 209-217 (1973).

3. F.R. Krüger and J. Kissel, Experimental investigations of ion emission with dust impact on solid surfaces, ESA SP-224, pp. 43-48 (1984).

4. F.R. Krüger, Ion emission on solid surfaces: comparison of dust impact with other excitations, ESA SP-224, pp. 49-54 (1984).

5. J. Kissel and F.R. Krueger, Ion formation by impact of fast dust particles and comparison with related techniques, *Appl. Phys. A* **42**, 69-85 (1987).

6. K. Hornung and J. Kissel, On shock wave impact ionization of dust particles, *Astron. and Astro.* **291**(1), 324-336 (1994).

7. F.R. Krueger, Thermodynamics of ion formation by fast dissipation of energy at solid surfaces, *Z. Naturforsch.* **38a**, 385-394 (1983).

8. J.F. Friichtenicht, N.L. Roy and D.G. Becker, The Cosmic Dust Analyzer: experimental evaluation of an impact ionization model, NASA SP-319, pp. 299-310 (1971).

9. P.R. Ratcliff and F. Allahdadi, Characteristics of the plasma from a 94 km s^{-1} micro-particle impact, *Adv. Space Res.* **17**(12), 87-91 (1996).

10. S.F. Green, C.D. Clarke and T.J. Stevenson, A 2MV Van de Graaff accelerator for cosmic dust impact simulation, *J. Brit. Interplanetary Soc.* **41** No. 9, 393-396 (1988).

11. M.J. Burchell, M.J. Cole, J.A.M. McDonnell and P.R. Ratcliff, The hypervelocity impact facilities at the University of Kent, UK. Lunar and Planetary Institute Technical Report 94-05, pp. 32-35 (1994).

12. E.L. Christiansen, E. Cykowski and J. Ortega, Highly oblique impacts into thick and thin targets, *Int. J. Impact Engng* **14**, 157-168 (1993).

13. N.G. Mackay, S.F. Green, D.J. Gardner and J.A.M. McDonnell, Experimental investigation of the relationship between impact crater morphology and impacting particle velocity and direction. In *LDEF - 69 Months in Space. Third Post-Retrieval Symposium*, Williamsburg, Virginia, November 8-12 1993. NASA CP-3275, pp. 499-508 (1993).

14. J.A.M. McDonnell, D.J. Gardner, P.J. Newman, N.J. Robertson and C.J. Hayhurst, Hydrocode modelling in the study of space debris impact crater morphology. In *Proc. 1st European Conf. on Space Debris*, Darmstadt, Germany, 5-7 April 1993. ESA SD-01, pp. 425-432 (1993).

15. C.J. Hayhurst, H.J. Ranson, D.J. Gardner and N.K. Birnbaum, Modelling of microparticle hypervelocity oblique impacts on thick targets, *Int. J. Impact Engng* **17**, 375-386 (1995).

16. J.R. Göller and E. Grün, Calibration of the Galileo/Ulysses dust detectors with different projectile materials and at varying impact angles, *Planet. Space Sci.* **37**, 1197-1206 (1989).

17. P.R. Ratcliff, F. Gogu, E. Grün and R. Srama, Plasma production by secondary impacts: implications for velocity measurements by in-situ dust detectors, *Adv. Space Res.* **17**(12), 111-115 (1996).

18. G. Eichhorn, Primary velocity dependence of impact ejecta parameters, *Planet. Space Sci.* **26**, 469-471 (1978).

19. P.R. Ratcliff, M.J. Cole, H.A. Shaw, J.A.M. McDonnell and F. Allahdadi, Experimental determination of energy partitioning in microparticle impacts at velocities from 1 to 100 km s^{-1}, Paper IAF-95-I.5.03 (1995).

20. B.-K Dalmann, E. Grün and J. Kissel, The ion-composition of the plasma produced by impacts of fast dust particles, *Planet. Space Sci.* **25**, 135-147 (1977).

21. F.R. Krüger and J. Kissel, Experimental investigations on ion emission with dust impact on solid surfaces, ESA SP-224, pp. 34-48 (1984).